

Article

# Effect of Vinylene Carbonate Electrolyte Additive on the Surface Chemistry and Pseudocapacitive Sodium-Ion Storage of TiO<sub>2</sub> Nanosheet Anodes

Rudi Ruben Maça<sup>1,2</sup>  and Vinodkumar Etacheri<sup>1,\*</sup> <sup>1</sup> Electrochemistry Division, IMDEA Materials Institute, 28906 Madrid, Spain; rudi.maca@imdea.org<sup>2</sup> Faculty of Science, Universidad Autónoma de Madrid, 28049 Madrid, Spain

\* Correspondence: vinodkumar.etacheri@imdea.org

**Abstract:** Although titanium dioxide has gained much attention as a sodium-ion battery anode material, obtaining high specific capacity and cycling stability remains a challenge. Herein, we report significantly improved surface chemistry and pseudocapacitive Na-ion storage performance of TiO<sub>2</sub> nanosheet anode in vinylene carbonate (VC)-containing electrolyte solution. In addition to the excellent pseudocapacitance (~87%), the TiO<sub>2</sub> anodes also exhibited increased high-specific capacity (219 mAh/g), rate performance (40 mAh/g @ 1 A/g), coulombic efficiency (~100%), and cycling stability (~90% after 750 cycles). Spectroscopic and microscopic studies confirmed polycarbonate based solid electrolyte interface (SEI) formation in VC-containing electrolyte solution. The superior electrochemical performance of the TiO<sub>2</sub> nanosheet anode in VC-containing electrolyte solution is credited to the improved pseudocapacitive Na-ion diffusion through the polycarbonate based SEI (coefficients of  $1.65 \times 10^{-14}$  for PC-VC vs.  $6.42 \times 10^{-16}$  for PC). This study emphasizes the crucial role of the electrolyte solution and electrode–electrolyte interfaces in the improved pseudocapacitive Na-ion storage performance of TiO<sub>2</sub> anodes.

**Keywords:** electrolyte; additive; interface; pseudocapacitance; intercalation; energy storage; secondary battery; sodium-ion

**Citation:** Maça, R.R.; Etacheri, V.Effect of Vinylene Carbonate Electrolyte Additive on the Surface Chemistry and Pseudocapacitive Sodium-Ion Storage of TiO<sub>2</sub> Nanosheet Anodes. *Batteries* **2021**, *7*, 1. <https://dx.doi.org/10.3390/batteries7010001>

Received: 20 November 2020

Accepted: 21 December 2020

Published: 24 December 2020

**Publisher's Note:** MDPI stays neutral with regard to jurisdictional claims in published maps and institutional affiliations.



**Copyright:** © 2020 by the authors. Licensee MDPI, Basel, Switzerland. This article is an open access article distributed under the terms and conditions of the Creative Commons Attribution (CC BY) license (<https://creativecommons.org/licenses/by/4.0/>).

## 1. Introduction

Lithium-ion batteries (LIBs) are widely used in the current generation of portable electronics, electric vehicles, and smart grids coupled with renewable energy sources [1–4]. Despite their high energy density, moderate power density, and good cycle life, there are concerns regarding the future large-scale implementation of LIBs due to the limited availability of expensive (\$17,000 per metric ton) lithium resources, where market demand will be up to two to six times extraction capacity in the next two decades [5,6]. Rechargeable sodium-ion batteries (SIBs) are very attractive in this regard, due to the abundance of inexpensive sodium resources [3,5,7,8]. Moreover, the similar electrochemistry and redox potentials of lithium and sodium (−3.02 and −2.71 V vs. SHE, respectively), make it a suitable candidate for efficient electrochemical energy storage [9–11]. However, the larger size of Na-ions compared to Li-ions (1.02 and 0.76 Å radius, respectively) hinders their intercalation in the most commonly used Li-ion battery anode material, graphite (interlayer d-spacing of 3.4 Å) [1,12,13]. Shuttling of solvated Na-ions between individual electrodes is also sluggish, leading to the poor rate performance and cycling stability of Na-ion batteries [14]. Hence, numerous studies have focused on the development of alternative high-performance anode materials [15–20].

Carbonaceous materials with large interlayer spacing, such as hard carbon, graphene, and amorphous carbon have been widely investigated as anode materials [16,17]. However, these anodes exhibited low specific capacities, poor rate performances, and mediocre cycling stability. Despite the high specific capacity of conversion (Co<sub>3</sub>O<sub>4</sub>, SnO<sub>2</sub>, Fe<sub>3</sub>O<sub>4</sub>,

NiO, CuO, MnO<sub>2</sub>, etc.) and alloying type (Sn, Ge, Sb, etc.) anodes, rapid capacity fading associated with huge volume changes make them less attractive for Na-ion battery applications [18–20]. Insertion type metal oxides, such as Nb<sub>2</sub>O<sub>5</sub>, Na<sub>2</sub>Ti<sub>3</sub>O<sub>7</sub>, TiO<sub>2</sub>, and Li<sub>4</sub>Ti<sub>5</sub>O<sub>12</sub> are another class of Na-ion battery anodes [21,22]. Titanium dioxide (TiO<sub>2</sub>) has received much attention among anode materials due to its high chemical stability, non-toxicity, abundance, low volume change during Na-ion intercalation, and inexpensive nature [23–26]. Amorphous and different crystalline (anatase, bronze, rutile, etc.) polymorphs of TiO<sub>2</sub> have been investigated as promising Na-ion battery anodes [7,27–30]. The existence of 2D intercalation channels in crystalline polymorphs make them superior to amorphous TiO<sub>2</sub> for Na-ion storage [4,9,31]. Hence, anatase TiO<sub>2</sub> composed of TiO<sub>6</sub> octahedra and zigzag edges of the 3-D network have become the most studied polymorph [4,32]. Bronze polymorph of TiO<sub>2</sub> has recently attracted a lot of attention as a Na-ion battery anode due to the presence of more open channels and layered crystal structure [29,33]. The Na-ion intercalation kinetics' dependence on crystal structure and orientation has also been proved in recent studies [22,33]. Nevertheless, TiO<sub>2</sub> anodes suffer from low electronic conductivity, mediocre specific capacity, poor rate-performance, and low cycling stability [25,34].

Numerous strategies such as carbon coating, doping with other transition metal ions, and the synthesis of different morphologies in the nanoscale have been established for improving the Na-ion storage performance of TiO<sub>2</sub> anodes [23,26,34]. Nevertheless, these methods have only resulted in a trivial improvement of specific capacities and cycling stabilities. Another advanced approach to improve the electrochemical performance is to increase the diffusion independent pseudocapacitive-type Na-ion storage [14,21]. This surface/near-surface ion storage is independent of the electronic and ionic conductivity of the electrode material [21]. In addition to the excellent rate performance and cycling stabilities, due to negligible structural changes during the charge–discharge process, high specific capacities can also be achieved due to the synergy with diffusion limited Na-ion storage [30,35]. Improved pseudocapacitance can usually be achieved by either precise nanostructuring, or the formation of hybrids with carbonaceous materials. These approaches were recently demonstrated for enhancing the intrinsic (~4%) pseudocapacitive Na-ion storage of TiO<sub>2</sub> anodes [22]. For instance Chen et al. demonstrated the excellent electrochemical performance of TiO<sub>2</sub>-nanosheets grown on RGO [36]. Our recent study demonstrated the significantly improved pseudocapacitance of nanointerface engineered anatase-bronze hybrid TiO<sub>2</sub> nanosheets [9]. The formation of additional Na-ion diffusion pathways, and efficient charge separation were responsible for the improved pseudocapacitance of these electrodes [37].

Solid electrolyte interface (SEI) characteristics are crucial in deciding the electrochemical performance, in addition to the physiochemical properties of an electrode material [38,39]. Carefully engineered electrode–electrolyte interfaces can enable producing batteries with superior energy/power densities and cycling stabilities [38,40]. Since SEIs are formed as a result of electrolyte decomposition, the most appropriate approach to engineer SEI properties is to tune the electrolyte composition [39,40]. Carbonate based electrolyte compositions usually contain solvents such as ethylene carbonate (EC), propylene carbonate (PC), ethyl methyl carbonate (EMC), etc., and a suitable sodium salt (NaPF<sub>6</sub>, NaTFSI, NaClO<sub>4</sub>, etc.). Electrochemical decomposition of these electrolytes results in the formation of an electrode–electrolyte interface composed of sodium alkyl carbonates, sodium alkoxides, polyenes, polycarbonates, and inorganic salts [5,38,41,42]. Excess electrolyte decomposition, due to the extreme reactivity of high surface area nanostructured electrodes, can often lead to increased SEI formation, which deteriorates the Na-ion storage performance [24,39]. Only a thin SEI layer capable of protecting the electrode from continuous reaction with the electrolyte solution is necessary to maintain optimal Na-ion diffusion, and a high degree of reversibility [43]. The chemical stability of SEI components is also critical to prevent dissolution in the electrolyte solution, which can lead to continuous SEI formation at the expense of electrolyte decomposition, and cell failure [38,41,44].

Using electrolyte additives is one widely employed strategy to endow the SEIs with superior electrochemical properties [40,44]. Vinylene carbonate (VC) is one of the most commonly used electrolyte additives in the case of Li-ion batteries [41,44,45]. This has been mainly aimed at flexible SEI formation in large volume expansion conversion/alloying type anodes, and at preventing metal-ion leaching from high voltage cathodes [38,42,46]. The high electrochemical reactivity of VC results in the preferential formation of polymeric SEIs, which prevent further reaction of the electrode material with the electrolyte solution during extreme operating environments, including high temperature, and large volume change [40,44,47]. Use of VC in the case of Na-ion batteries is also mainly aimed at improving the cycling stability of high capacity conversion/alloying type anodes [46]. However, none of these studies investigated SEI composition tuning to enhance the pseudocapacitive Na-ion storage of TiO<sub>2</sub> anodes.

Herein, we report significantly improved pseudocapacitive Na-ion storage and surface chemistry of TiO<sub>2</sub> nanosheet anodes in VC-containing electrolyte solution. Vinylene carbonate, a widely used Li-ion battery additive was chosen in this case due to its ability to form SEIs with superior passivation and Na-ion diffusion properties. The presence of a double bond is mainly responsible for the preferential decomposition/polymerization of VC associated with the generation of polycarbonate based SEIs. Ultrathin, mesoporous, and high surface area TiO<sub>2</sub> nanosheets were selected as the preferred anode material in this case, to improve the contact with the electrolyte solution and thereby amplify the effect of the electrolyte additive on the surface chemistry and electrochemical performance. The excellent electrochemical performance of TiO<sub>2</sub> nanosheet anode in VC-containing electrolyte solution is credited to the superior pseudocapacitance, resulting from the faster Na-ion diffusion through the polycarbonate based surface film.

Figure 1 shows the different solid electrolyte interface (SEI) composition on TiO<sub>2</sub> nanosheet anodes formed in vinylene carbonate (VC)-containing and VC-free electrolyte solutions.

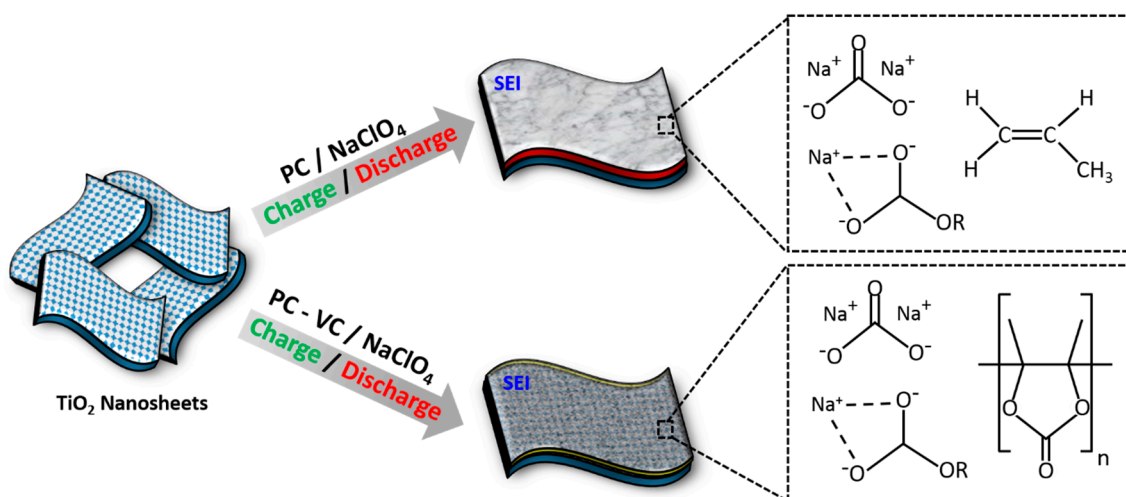


**Figure 1.** Schematic of the different solid electrolyte interface (SEI) composition on TiO<sub>2</sub> nanosheet anodes formed in vinylene carbonate (VC)-containing and VC-free electrolyte solutions.

## 2. Experimental

### 2.1. Materials Synthesis

TiO<sub>2</sub> nanosheets were synthesized through a solvothermal method [48]. In a typical synthesis, 4 mL of deionized water and 20% aqueous TiCl<sub>3</sub> (99.99%, Acros Organics) each were added dropwise in 50 mL of ethylene glycol (99.99%, Fisher Scientific) under continuous stirring. The dark brown solution was then heated to 150 °C for 6 h in a PTFE-lined stainless steel autoclave. The subsequent slurry was washed several times with

deionized water and ethanol, and dried at 80 °C for 24 h to obtain bronze TiO<sub>2</sub> (TiO<sub>2</sub>-B) nanosheets. Hierarchical anatase-bronze hybrid TiO<sub>2</sub> nanosheets were obtained by heat-treating TiO<sub>2</sub>-B nanosheets at 400 °C for 2 h under air flow (heating and cooling rates of 10 °C/min).

## 2.2. Materials Characterization

X-ray diffraction (XRD) patterns of the samples were collected using a PANalytical Empyrean high-resolution diffractometer equipped with a Cu-K $\alpha$  X-ray source ( $\lambda = 1.5406 \text{ \AA}$ ). The average crystallite size of the TiO<sub>2</sub> nanosheets was calculated using the Debye–Scherrer equation ( $D = K \lambda / \beta \cos\theta$ ), where  $D$  is particle size,  $K$  is the shape factor 0.9,  $\lambda$  is the wavelength of the X-ray radiation of Cu-K $\alpha$ , and  $\beta$  is the full width at half maximum (FWHM) of the highest intensity peak. Room temperature Raman analysis was performed with a Renishaw PLC Raman spectrometer equipped with a 532 nm Nd: YAG laser. Sample damage was avoided by limiting the laser power to 5 mW. FTIR spectra of pristine and cycled electrodes after washing with anhydrous acetonitrile (Sigma-Aldrich, 99.9%) were recorded using a Thermo Scientific Nicolet iS50 in attenuated total reflectance (ATR) mode, in the range of 4000–400 cm<sup>-1</sup>. FTIR spectra of pristine, cycled and non-washed electrodes were also collected for comparison. Microstructural characterization of TiO<sub>2</sub> nanosheets was performed using a scanning electron microscope (FEI Helios NanoLab 600i) and high-resolution transmission electron microscope (FEI Talos F200X FEG). X-ray photoelectron spectroscopy (XPS) measurements were performed using a SPECS PHOIBOS 150 9MCD instrument equipped with a Multi-Channeltron detector and a monochromatic X-ray source of twin Mg anodes. The binding energies of elements in the XPS spectra were set accordingly to the CC/CH component of the C 1s peak at 284.8 eV. For the quantitative analysis of SEI, high-resolution core-level spectra were used after removing the nonlinear Shirley background.

## 2.3. Electrochemical Measurements

A Vigor glovebox filled with high-purity ( $\geq 99.999\%$ ) Ar-gas (H<sub>2</sub>O and O<sub>2</sub> < 1.0 ppm) was used to fabricate 2032 type Na-ion half-cells. Metallic sodium foil was used for the counter and reference electrodes. The separator consisted of Whatman glass fiber (GF/B type) soaked in 1 M NaClO<sub>4</sub> ( $\geq 98.0\%$ , Sigma-Aldrich), in propylene carbonate (PC, 99.7%, Sigma-Aldrich), and 3% vinylene carbonate (VC, 97%, Sigma-Aldrich). Working electrodes contained 70wt.% TiO<sub>2</sub> nanosheets, 20wt.% acetylene black (MTI Chemicals), and 10wt.% of polyvinylidene fluoride (PVDF, MW: 600.000, MTI Chemicals) binder. N-methylpyrrolidone (NMP, 99.9%, Aladdin Chemicals) solvent was used for preparing the slurry containing the active material, conductive additive, and binder, followed by coating on a 10  $\mu\text{m}$  thick copper foil. Working electrodes consisted of an active material loading of 2–3 mg/cm<sup>2</sup>. A Neware BTS4000 model multichannel battery tester was employed to galvanostatically cycle the assembled half-cells between 0.01–3.0 V (vs. Na<sup>+/0</sup>) at 25 °C. Specific capacities were expressed, calculated according to the active material weight, within a 3% error limit. A ZIVE SP1 electrochemical workstation was used for electrochemical impedance spectroscopy (EIS) measurements (1 MHz to 10 mHz) and for cyclic voltammetry (CV) measurements (0.1 to 100 mV/s). EIS measurements were performed using a 3-electrode coin-cell configuration. Diffusion-controlled and diffusion-independent processes were calculated according to Equation (1).

$$i(V) = k_1 v + k_2 v^{\frac{1}{2}} \quad (1)$$

$k_1 v$  and  $k_2 v^{\frac{1}{2}}$  represent current contributions for diffusion-independent and diffusion-controlled processes, respectively.  $k_1$  and  $k_2$  coefficients are the slope and intercept from the

linear fit of the plot  $i(V)$  vs.  $v$ , respectively. Na-ion diffusion coefficients of  $\text{TiO}_2$  nanosheets were determined using Equation (2).

$$D = \frac{1}{2} \left( \frac{RT}{AF^2\sigma_w C} \right)^2 \quad (2)$$

where  $D$  is Na-ion diffusion coefficient at absolute temperature  $T$ , and  $R$  denotes the gas constant. Faraday's constant, Na-ion concentration in electrolyte, and electrode area are represented as  $F$ ,  $C$  and  $A$ , respectively. Warburg impedance,  $\sigma_w$ , was calculated from the slope of the linear plot of  $Z'$  vs.  $\omega^{-1/2}$ .

### 3. Results and Discussion

#### 3.1. Synthesis and Characterization of $\text{TiO}_2$ Nanosheets

Hierarchical  $\text{TiO}_2$  nanosheets composed of anatase and bronze nanocrystallites were synthesized through a solvothermal method, followed by controlled heat treatment. Ethylene glycol was used as solvent to facilitate nanosheet formation through the interaction of OH groups of glycol with Ti-OH groups [48,49]. This resulted in the free energy change of the  $\text{TiO}_2$  crystallographic planes and an associated anisotropic crystal growth [29,49]. Selection of a less reactive precursor  $\text{TiCl}_3$  was aimed at controlled hydrolysis and condensation, which is necessary for the nanosheet formation [50]. The uniform size/shape distributions and ultrathin nature of the sheets were also assisted by the high viscosity of ethylene glycol [9]. Reaction between  $\text{TiCl}_3$  and ethylene glycol resulted in the formation of Ti-glycolate complex during the hydrothermal reaction. Further hydrolysis and condensation formed  $\text{TiO}_2$  bronze nanosheets, which was transformed to anatase-bronze hybrid nanosheets upon controlled heat treatment. Scanning electron microscopy (SEM) images of the  $\text{TiO}_2$  nanosheets demonstrated their 2D morphology and (Figure 2a) hierarchical flower like microstructure, composed of numerous petals. High-resolution transmission electron microscopy (TEM) images (Figure 2b,c) of individual nanosheets verified the existence of nanograins of  $7 \pm 2$  nm size. Lattice spacings of 0.34 and 0.62 nm represent the (101) and (110) planes of anatase and bronze phases, respectively. The presence of well-defined anatase-bronze nanograin boundaries is also evident from these images [9]. This was anticipated, due to the mismatch between anatase and bronze crystal structures. Nanograin boundaries present in metal oxides often result in unique physical/ chemical properties, including excellent catalytic and electrochemical performance [51]. Nanointerfaces present in these hierarchical  $\text{TiO}_2$  nanosheets can also act as additional sites for Na-ion storage. Our previous study confirmed the advantages of such nanointerfaces for enhancing pseudocapacitive type Na-ion storage [9].

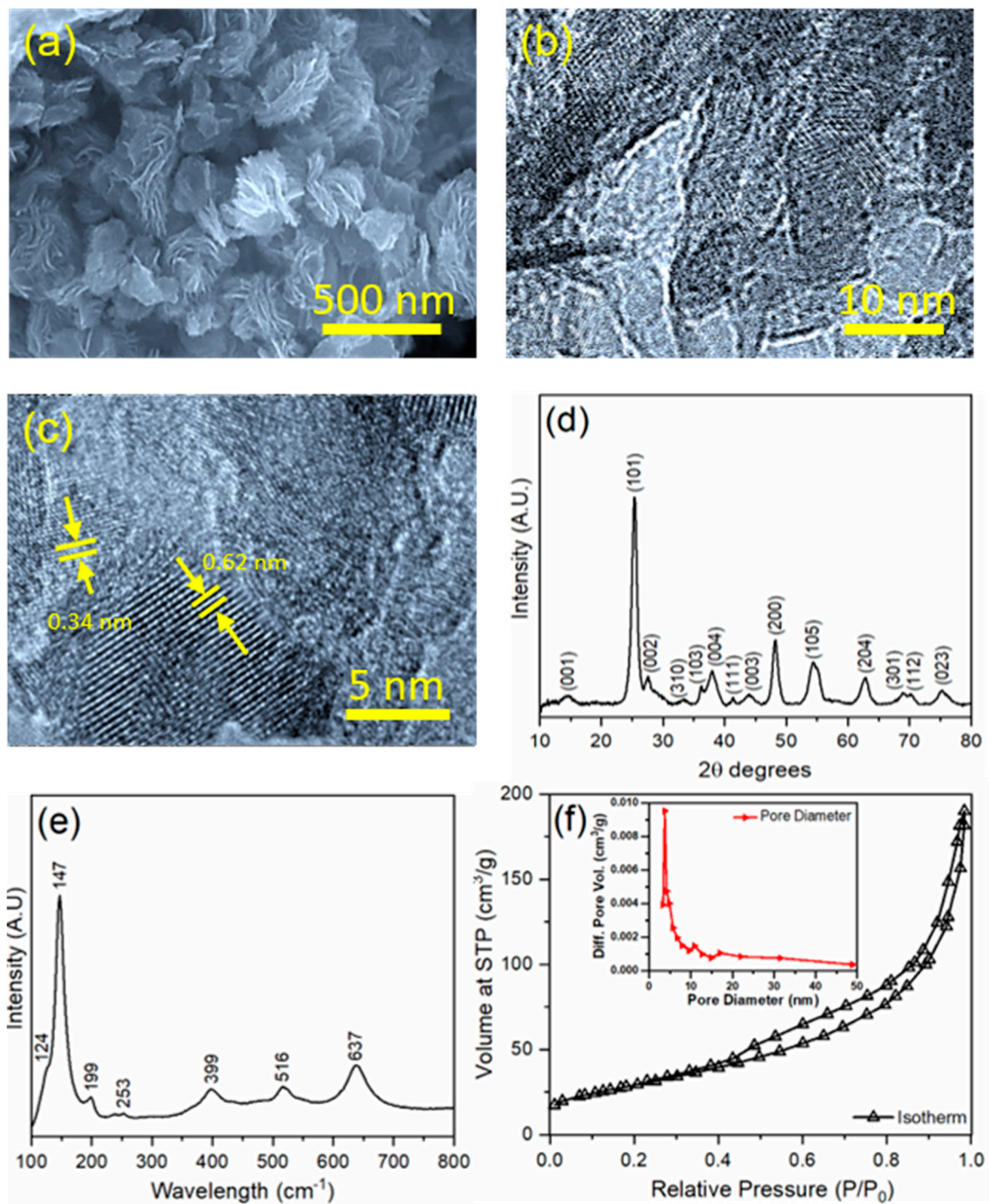


**Figure 2.** (a) SEM image, (b,c) TEM images, (d) X-ray diffraction pattern, (e) Raman spectrum, (f)  $N_2$  adsorption–desorption isotherm, and pore size distribution (inset) of  $TiO_2$  nanosheets.

The X-ray diffraction pattern of the  $TiO_2$  nanosheets (Figure 2d) also confirmed the coexistence of anatase and bronze polymorphs in the sample. Peaks designated as (101), (004), (200), (105), (211), (204) corresponded to anatase phase (JCPDS 21–1272). Whereas, (001), (110), (002), (310), (103), (003), and (204) signals represented bronze phase (JCPDS 46–1237) [9]. The anatase and bronze content, calculated from the relative intensity of the (310) bronze peak and (004) anatase peak, was found to be 83% and 17%, respectively. Particle size calculation, using a Debye–Scherrer equation also revealed the existence of

$7 \pm 2$  nm sized crystallites, which was in good agreement with the TEM results. A more surface sensitive technique, Raman spectroscopy was used to further confirm the phase purity and uniform nanoscale distribution of the anatase and bronze polymorphs (Figure 2e). Raman active modes were 144, 197, 399, 514, and  $639 \text{ cm}^{-1}$  for anatase, and 123, 145, 161, 172, 196, 201, and  $259 \text{ cm}^{-1}$  for bronze polymorphs [52]. These results and the quantification of anatase/bronze content from high-resolution Raman spectra (Figure S1) were also in line with the XRD results, confirming the coexistence and nanoscale distribution of anatase and bronze nanocrystallites [52]. The textural property investigation of  $\text{TiO}_2$  nanosheets was performed through  $\text{N}_2$  adsorption–desorption analysis (Figure 2f). This active material exhibited a high surface area of  $106 \text{ m}^2/\text{g}$ . Type IV isotherms and H3 type hysteresis, characteristic of a mesoporous structure were identified in this case [13]. Mesoporosity was also evidenced by the higher steepness of the isotherm at high relative pressure ( $P/P_0 = 0.4\text{--}1.0$ ) [13]. Barrett-Joyner-Halenda (BJH) method pore size distribution measurements (Figure 2f inset) further confirmed the mesoporosity of the  $\text{TiO}_2$  nanosheets. Such high surface area and mesoporosity of the active material are advantageous for improved Na-ion storage due to the superior contact with the electrolyte solution, and the possibility of pore/defect assisted pseudocapacitive type ion storage [49]. Thus, it can be summarized that controlled hydrolysis and condensation of  $\text{TiCl}_3$  in ethanol water mixture followed by calcination resulted in the formation of mesoporous hierarchical anatase–bronze hybrid  $\text{TiO}_2$  nanosheets.

### 3.2. Electrochemical Performance of the $\text{TiO}_2$ Nanosheets

The sodium-ion storage electrochemical performance of the  $\text{TiO}_2$  nanosheets was investigated in VC-containing (PC-VC/ $\text{NaClO}_4$ ) and VC-free (PC/ $\text{NaClO}_4$ ) electrolyte solutions. Second galvanostatic voltage profiles at different current densities (Figure 3a,b) indicated the marginally superior specific capacities of the  $\text{TiO}_2$  nanosheet anodes in PC-VC/ $\text{NaClO}_4$  electrolyte at various charge–discharge rates. First cycle coulombic efficiencies of 36% and 44.5% were observed in the PC/ $\text{NaClO}_4$  and PC-VC/ $\text{NaClO}_4$  electrolyte solutions, respectively (Figure S2). Irreversible capacity loss in the first cycle was attributed to unavoidable electrolyte decomposition, and irreversible  $\text{Na}_2\text{O}$  formation associated with sodiation. Coulombic efficiency reached  $\sim 100\%$  after the first charge–discharge in PC-VC/ $\text{NaClO}_4$  electrolyte, demonstrating the complete formation of high quality SEI during the first cycle. However, coulombic efficiency never reached  $\sim 100\%$  on extended cycling in PC/ $\text{NaClO}_4$  electrolyte, which indicated the formation of an SEI with inferior passivation properties. This is also apparent from the consecutive cyclic voltammograms presented (Figure 3c,d). The  $\text{TiO}_2$  nanosheet anodes exhibited a similar electrochemical response, irrespective of the electrolyte composition. Three different electrochemical processes constitute the first cathodic response in both systems. The high-voltage region between 2.25 and 0.7 V represents diffusion-independent pseudocapacitive Na-ion intercalation [53]. SEI formation resulting from the electrolyte decomposition could be identified from the cathodic response between 0.7 and 0.5 V [9]. Lack of this signal in the second cathodic scan confirmed complete SEI formation in the first charge–discharge cycle [32,54]. A low voltage region between 0.2 and 0 V corresponded to the diffusion controlled Na-ion intercalation into the anatase and bronze crystal structure [36]. These electrochemical responses were in line with the plateau at low potential and sloping voltage profiles. Anodic response in the voltage range of 0.2 V, and a broad signal between 0.5 and 2.25 V represented Na-ion deintercalation through pseudocapacitive and diffusion dependent process, respectively.

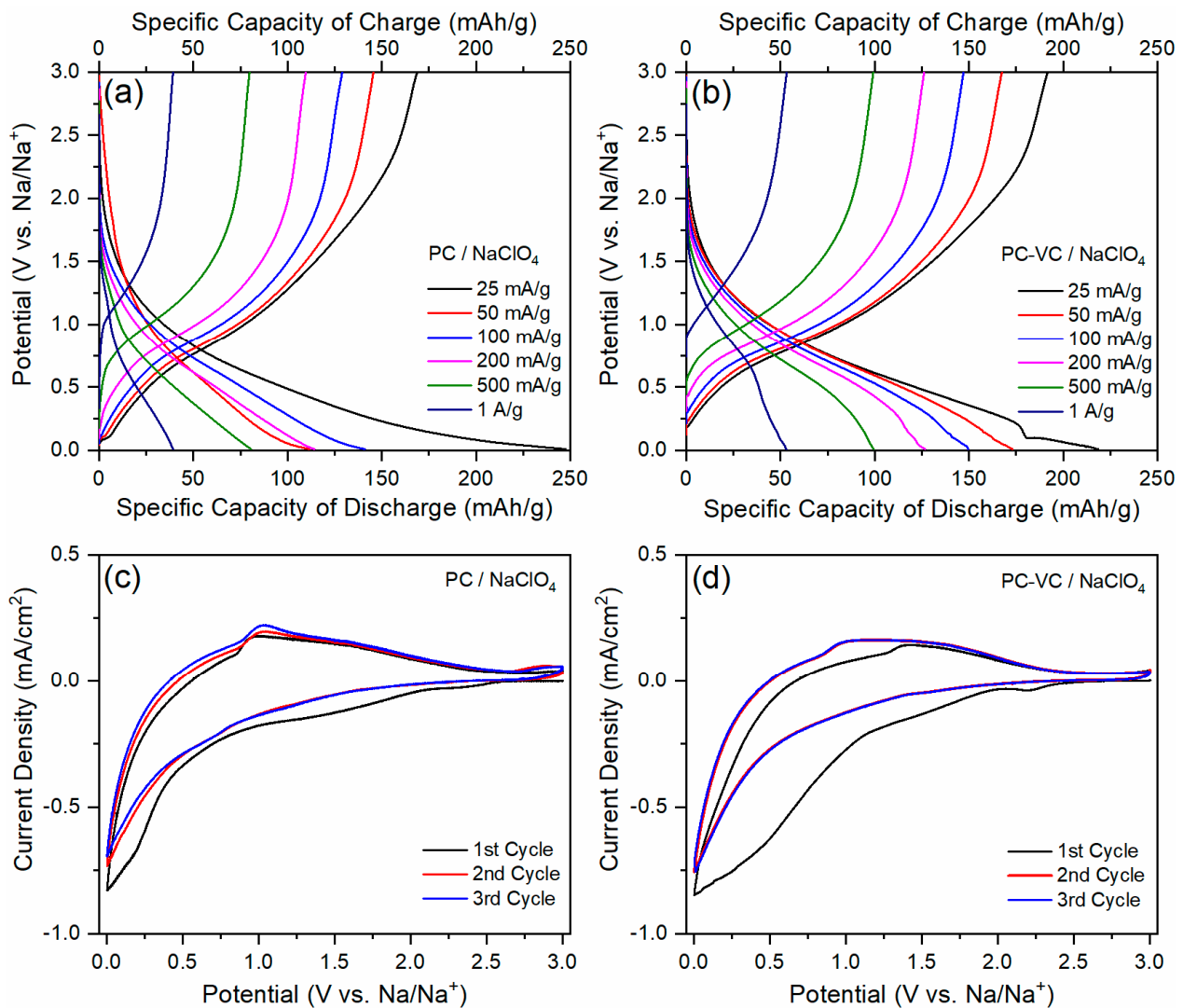


**Figure 3.** Galvanostatic voltage profiles of  $\text{TiO}_2$  nanosheet anodes in Na-ion half-cells containing: (a) PC/ $\text{NaClO}_4$ , and (b) PC-VC/ $\text{NaClO}_4$  electrolyte solutions at various current densities. Cyclic voltammograms of  $\text{TiO}_2$  nanosheet anodes at a scan rate of 1 mV/s in (c) PC/ $\text{NaClO}_4$ , and (d) PC-VC/ $\text{NaClO}_4$  electrolyte solution.

Sodiation over a wide voltage range was observed in this case, which was noticeably different from the intercalation reaction at specific potentials for previously reported  $\text{TiO}_2$  anodes [27]. Distinct Na-ion storage was also evidenced by the marginally different shape of the voltammograms compared to earlier reports [37]. Although cathodic signals corresponding to SEI formation disappeared in the first cycle, there was a clear indication of irreversibility and incomplete SEI formation during the consecutive cycles of the VC-free battery, which was not observed in the case of the VC-containing Na-ion half-cells. This was a clear indication of efficient SEI formation on the  $\text{TiO}_2$  nanosheet anodes in the VC-containing electrolyte solution. Thus, disappearance of the SEI formation peak in the first cycle and stable consecutive cycles confirmed the highly reversible Na-ion intercalation reactions of the  $\text{TiO}_2$  nanosheet anodes in VC-containing electrolyte solution. The galvanostatic rate performance of the  $\text{TiO}_2$  nanosheet anodes in both VC-free and VC-containing electrolyte solutions is presented in Figure 4a. Second cycle specific capacities were 247 and 219 mAh/g, respectively. Slightly higher capacities were identified in the case of VC-containing electrolyte solution during the following cycles at 25 mA/g. Capacity differences became more prominent at higher current densities, and also increased on reducing the current density to 25 mA/g. This was a clear indication of the capacity fading

of TiO<sub>2</sub> anode in VC-free electrolyte, which was further verified during the extended galvanostatic cycling (Figure 4b).

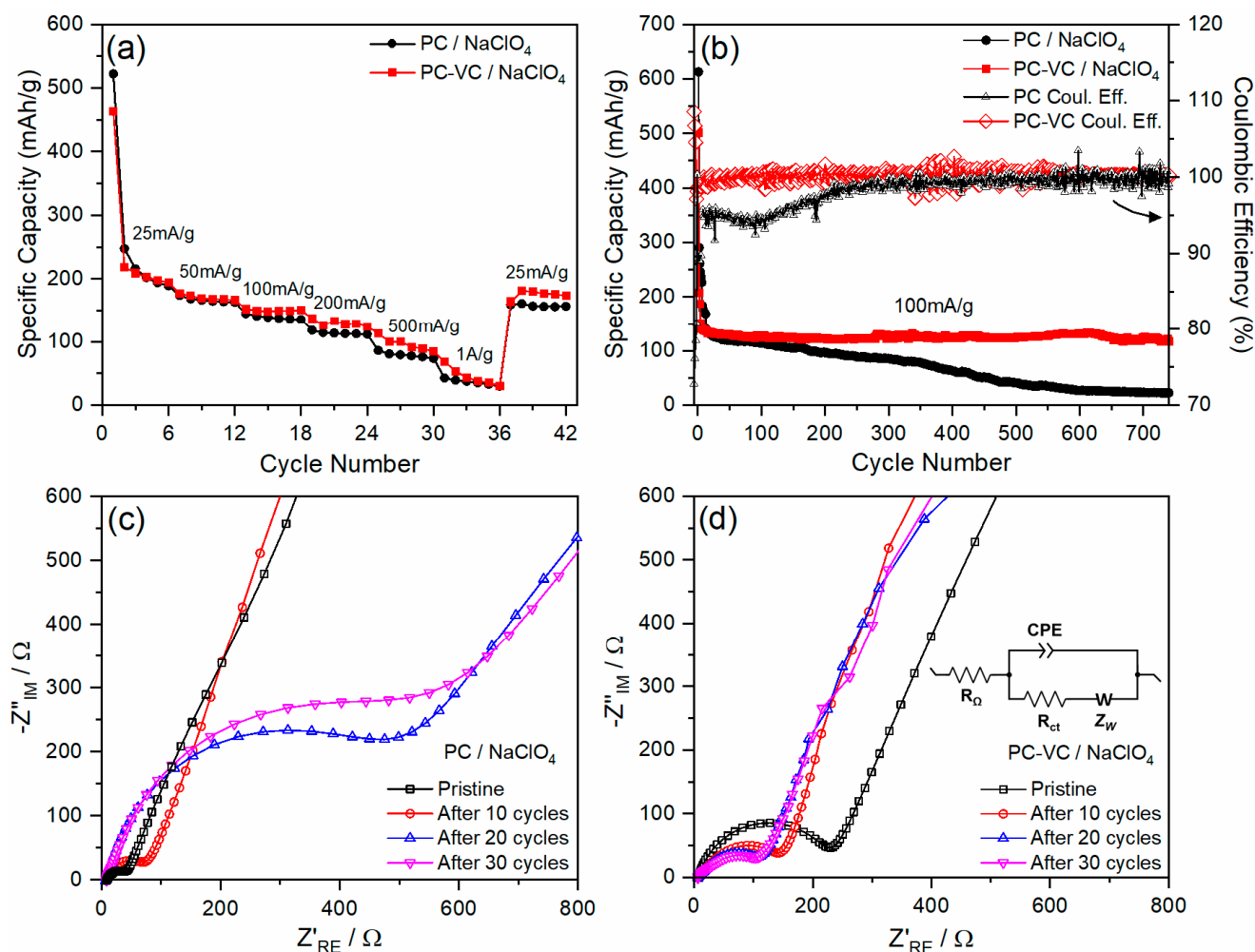


**Figure 4.** (a) Galvanostatic rate performance, and (b) cycling performance of TiO<sub>2</sub> nanosheet anodes in PC/NaClO<sub>4</sub> and PC-VC/NaClO<sub>4</sub> electrolyte solutions. Nyquist plots and equivalent circuit (inset) of TiO<sub>2</sub> nanosheets in (c) PC/NaClO<sub>4</sub> and (d) PC-VC/NaClO<sub>4</sub> electrolyte solutions.

Both cells demonstrated ~100% coulombic efficiency after 750 cycles at a current density of 100 mA/g. Galvanostatic long-cycling performance of electrolyte solutions containing different amounts of VC confirmed 3% as the optimum concentration (Figure S3). For instance, at a current density of 100 mA/g, TiO<sub>2</sub> nanosheet anode in Na-ion half-cell configuration retained 90% of the initial capacity, with ~100% coulombic efficiency after 750 galvanostatic charge–discharge cycles. On the other hand, Na-ion half-cells containing VC-free electrolyte solution retained only 16% of the initial capacity, with ~98% coulombic efficiency.

Electrochemical impedance spectroscopy (EIS) of pristine and cycled electrodes (Figure 4c,d) is performed to gain further insights into the effect of SEI films on the charge transfer, and Na-ion diffusion characteristics. High-to-medium frequency part of the EIS pattern can be assigned to the sum of SEI/contact resistance and charge-transfer resistance and represented as  $R_{\Omega}$  and  $R_{ct}$  respectively in the Randles-like equivalent circuit (Figure 4d inset). Low frequency sloping line corresponds to solid-state diffusion kinetics of Na-ions shown as Warburg impedance ( $Z_w$ ) while constant phase element (CPE) is used to model the surface storage of Na-ions [7,49,55]. Charge transfer resistances of pristine TiO<sub>2</sub> nanosheet anodes in VC-free and VC-containing electrolyte solutions, obtained by fitting

the Nyquist plot to the equivalent circuit, are  $39 \Omega$  and  $171 \Omega$  respectively. It is interesting to observe such impedance difference in pristine batteries as VC is supposed to influence SEI formation only during the first charge-discharge cycle. This could be related to the spontaneous SEI formation resulting from the increased reactivity of high surface area  $\text{TiO}_2$  nanosheets with the electrolyte solution even in the absence of applied potential. Such surface film formations were also observed previously in the case of pyrolytic graphite, carbon and silicon nanowire electrodes [41,56,57]. Charge transfer resistance in VC-free electrolyte solution increased to  $517 \Omega$  after 30 galvanostatic cycles. In contrast, resistance decreased to  $105 \Omega$  in the case of VC-containing half-cells. Na-ion diffusion coefficients of  $\text{TiO}_2$  nanosheet anodes after 30 galvanostatic cycles in VC-free and VC containing electrolyte solutions calculated from the Nyquist plot are  $6.42 \times 10^{-16}$  and  $1.65 \times 10^{-14}$  correspondingly. Hence it is clear that VC-addition significantly reduces the charge transfer resistance and enhances the Na-ion diffusion kinetics, facilitating improved Na-ion diffusion into the  $\text{TiO}_2$  nanosheets. These results are also in good agreement with the superior cycling performance of  $\text{TiO}_2$  nanosheet electrodes in VC-containing electrolyte solution.

The sodium-ion storage mechanism of  $\text{TiO}_2$  nanosheets in VC-free and VC-containing electrolyte solutions was further investigated by collecting cyclic voltammograms at various scan rates (Figure 5a,b). Considerable differences existed in the voltammograms in the two different electrolyte solutions. High peak current and area were identified for the  $\text{TiO}_2$  nanosheets in the VC-containing electrolyte, which is in line with their improved Na-ion storage performance observed from the galvanostatic rate performance and cycling studies. The shapes of the voltammograms were also different suggesting different Na-ion storage mechanisms. Anodic and cathodic current increased with an increase of scan rate in both electrolyte solutions, which is indicative of pseudocapacitive type Na-ion storage [21].

Sodium ion intercalation of  $\text{TiO}_2$  nanosheets, especially at higher scan rates, occurs over a wide voltage range in VC-containing electrolyte solution. Such broad signals indicate the increased diffusion independent behavior of Na-ion intercalation, which is typical in capacitive type electrode materials [58].

The sodium-ion storage of  $\text{TiO}_2$  nanosheet anodes consists of both diffusion limited and surface controlled process [59]. These components can be differentiated from the relationship between peak current density and scan rates, as presented in Equation (3) [21]

$$i = av^b \quad (3)$$

where current shown as  $i$ , the scan rate as  $v$ , and  $a$  and  $b$  are adjustable variables. If  $b = 0.5$ , storage process is identified as diffusion-controlled, and surface controlled if  $b = 1.0$  [60]. Moreover, as the Randles–Ševčík equation dictates, the increase of current is proportional to the square root of scan rate [55,61,62]. The slope of peak current density vs. scan rate plot (Figure 5c,d) represented dominant pseudocapacitive type Na-ion storage (increased slope) in  $\text{TiO}_2$  nanosheets, with a high degree of pseudocapacitance in the PC-VC/ $\text{NaClO}_4$  electrolyte solution.

The diffusion limited and pseudocapacitive contributions of specific capacities were quantified to further investigate the effect of electrolyte solutions on the Na-ion storage mechanism. Capacitive and diffusion controlled contributions of Na-ion half-cells containing PC/ $\text{NaClO}_4$  and PC-VC/ $\text{NaClO}_4$  electrolyte solutions at different scan rates are presented in Figure 6a,b.  $\text{TiO}_2$  nanosheet anode exhibited superior pseudocapacitive Na-ion storage in PC-VC/ $\text{NaClO}_4$  electrolyte solution (83% @ 1 mV/s) compared to PC/ $\text{NaClO}_4$  (63% @ 1 mV/s). Capacitance calculations were also performed after 30 galvanostatic cycles (Figure 6c,d) in order to investigate the capacity fading on extended cycling. The pseudocapacitance contribution of the  $\text{TiO}_2$  nanosheets reduced considerably (37% @ 1 mV/s), and slightly increased (87% @ 1 mV/s) in the PC/ $\text{NaClO}_4$  and PC-VC/ $\text{NaClO}_4$  electrolyte solutions, respectively (Figure 6e,f). The entirely different shape of the cyclic voltammograms also signified different Na-ion storage mechanisms in these  $\text{TiO}_2$  nanosheet anodes during extended cycling. It is worth noting that these results are in agreement with the EIS results presented earlier, where the impedance of the  $\text{TiO}_2$  anodes continually increased during

galvanostatic cycling in PC/NaClO<sub>4</sub>, and decreased in the PC-VC/NaClO<sub>4</sub> electrolyte solutions. These observations led to the conclusion that the SEI formed in the VC-containing electrolyte solutions facilitated improved pseudocapacitive Na-ion diffusion into the TiO<sub>2</sub> nanosheet anode. Hence, it is clear that the electrolyte composition played a crucial role in the cycling stability, impedance, and Na-ion storage mechanism of the TiO<sub>2</sub> nanosheet anodes.

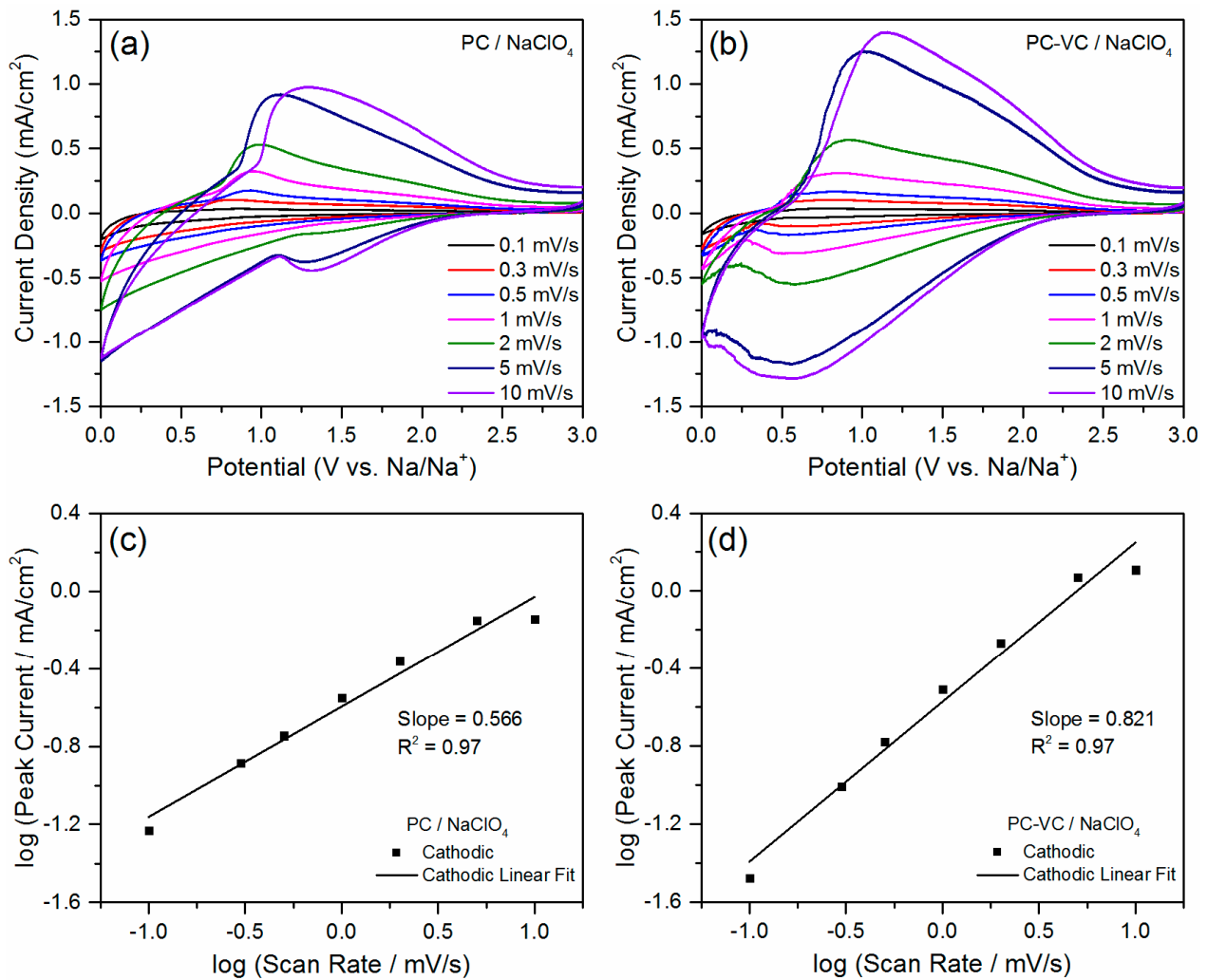


**Figure 5.** Cyclic voltammograms of TiO<sub>2</sub> nanosheet anodes at various scan rates in (a) PC/NaClO<sub>4</sub> and, (b) PC-VC/NaClO<sub>4</sub> electrolyte solutions. Scan rate dependence of peak current density for TiO<sub>2</sub> nanosheet anodes in (c) PC/NaClO<sub>4</sub>, and (d) PC-VC/NaClO<sub>4</sub> electrolyte solutions.

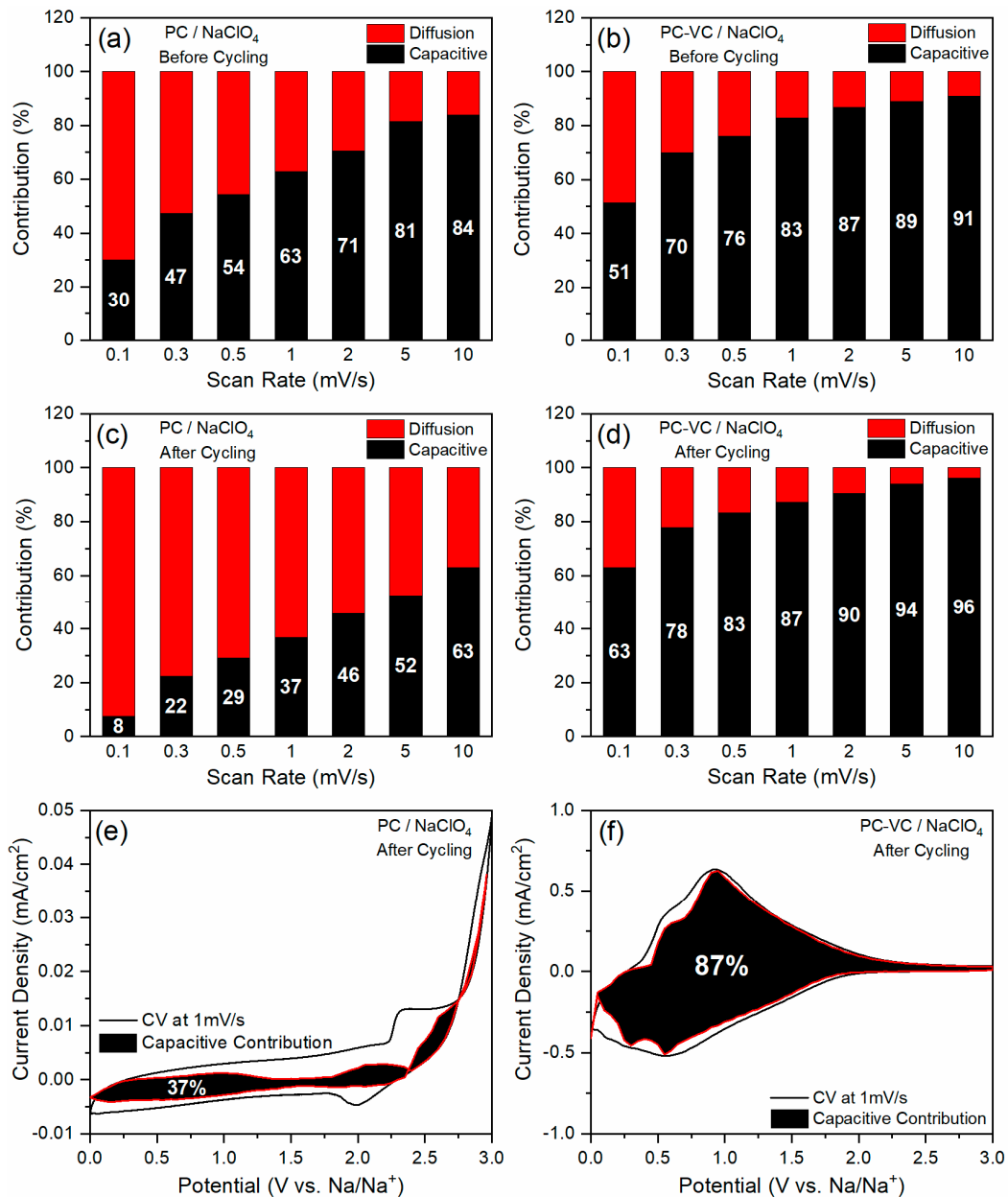


**Figure 6.** Pseudocapacitance contributions of the TiO<sub>2</sub> nanosheet anodes (a,b) before cycling, and (c,d) after cycling in PC/NaClO<sub>4</sub> and PC-VC/NaClO<sub>4</sub> electrolyte solutions. Pseudocapacitance contributions at a scan rate of 1 mV/s after 30 cycles in (e) PC/NaClO<sub>4</sub>, and (f) PC-VC/NaClO<sub>4</sub> electrolyte solutions.

### 3.3. Surface Chemical Characterization of TiO<sub>2</sub> Nanosheets

It is crucial to understand the surface chemistry of TiO<sub>2</sub> nanosheet electrodes cycled in VC-free and VC-containing electrolyte solutions due to the significant role of surface films on electrochemical performance. Surface chemical characterizations of these electrodes cycled in PC/NaClO<sub>4</sub> and PC-VC/NaClO<sub>4</sub> electrolyte solutions were performed using ex-situ XPS and FTIR techniques. Electrodes were thoroughly washed with acetonitrile and dried under vacuum to make sure that there was no residual NaClO<sub>4</sub> salt and solvent left to interfere with these spectroscopic measurements. The quantification of elements present in the surface films formed in VC-free and VC-containing electrolyte solutions (Table 1) indicated the contribution of both solvent and Na-salt towards SEI formation. Higher oxygen and carbon concentrations found in the surface film confirmed solvent

reduction as the major reaction responsible for SEI formation. Surface films formed in VC-containing electrolyte had a higher carbon and oxygen content, signifying the increased formation of numerous oxygen containing species, such as Na-carbonate, Na-alkyl carbonate, Na-alkoxides, and Na-polycarbonates, due to PC and VC reduction [63]. Lower Na and Cl content in this case was a clear indication of reduced Na-salt decomposition, which is vital to maintain good ionic conductivity during extended cycling. Increased Ti-content signifies the formation of surface films that allow superior X-ray/ electron penetration and detection of Ti-atoms underneath.

**Table 1.** Quantification of elements present in the TiO<sub>2</sub> nanosheet electrode surface film after 30 cycles in VC-containing and VC-free electrolyte solutions (based on XPS measurements).

Composition	C Content (at.%)	O Content (at.%)	Cl Content (at.%)	Na Content (at.%)	Ti Content (at.%)
PC/NaClO <sub>4</sub>	21.101	33.412	0.706	44.590	0.191
PC-VC/NaClO <sub>4</sub>	27.711	37.928	0.496	33.614	0.251

XPS spectra of the elements of interest present in the TiO<sub>2</sub> anode surface films formed in both electrolyte solutions (PC/NaClO<sub>4</sub> and PC-VC/NaClO<sub>4</sub>) are presented in Figures 7 and 8. These spectra demonstrated a significant difference in the chemical composition of surface films. Alkyl carbonate solvents (PC and VC in this case) can be easily reduced to organic and inorganic Na-salts under an applied potential [64].

### PC / NaClO<sub>4</sub>

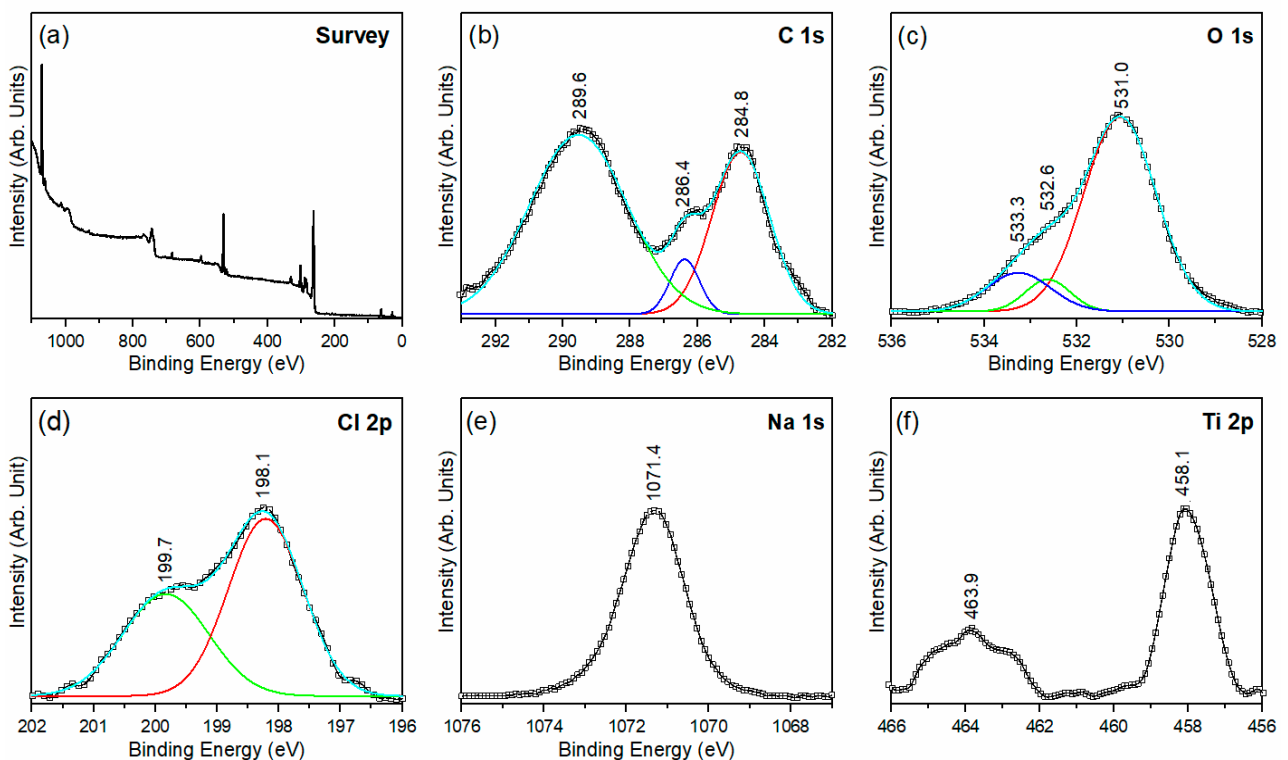


**Figure 7.** High-resolution XPS spectra of TiO<sub>2</sub> nanosheet electrodes after 30 cycles in PC/NaClO<sub>4</sub> electrolyte solution for (a) survey, (b) C 1s, (c) O 1s, (d) Cl 2p, (e) Na 1s, (f) Ti 2p.

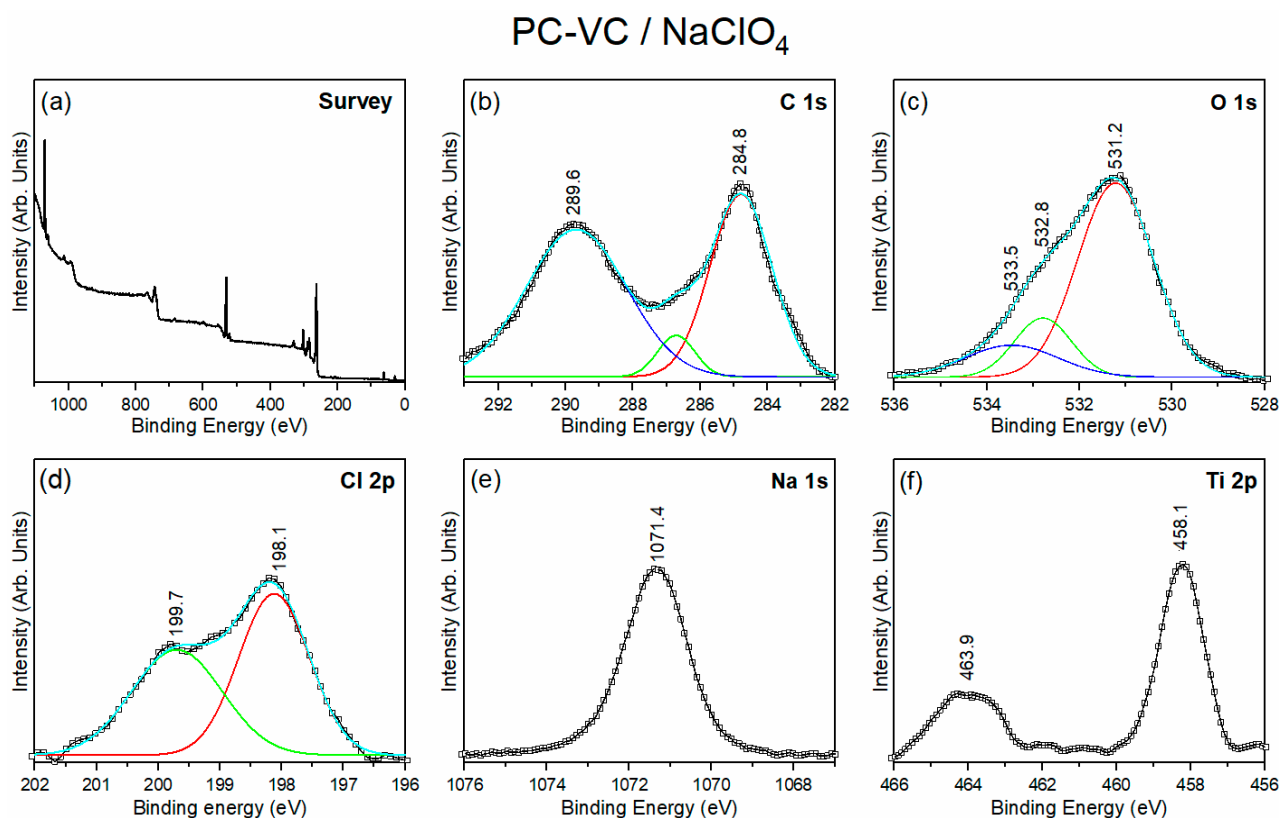
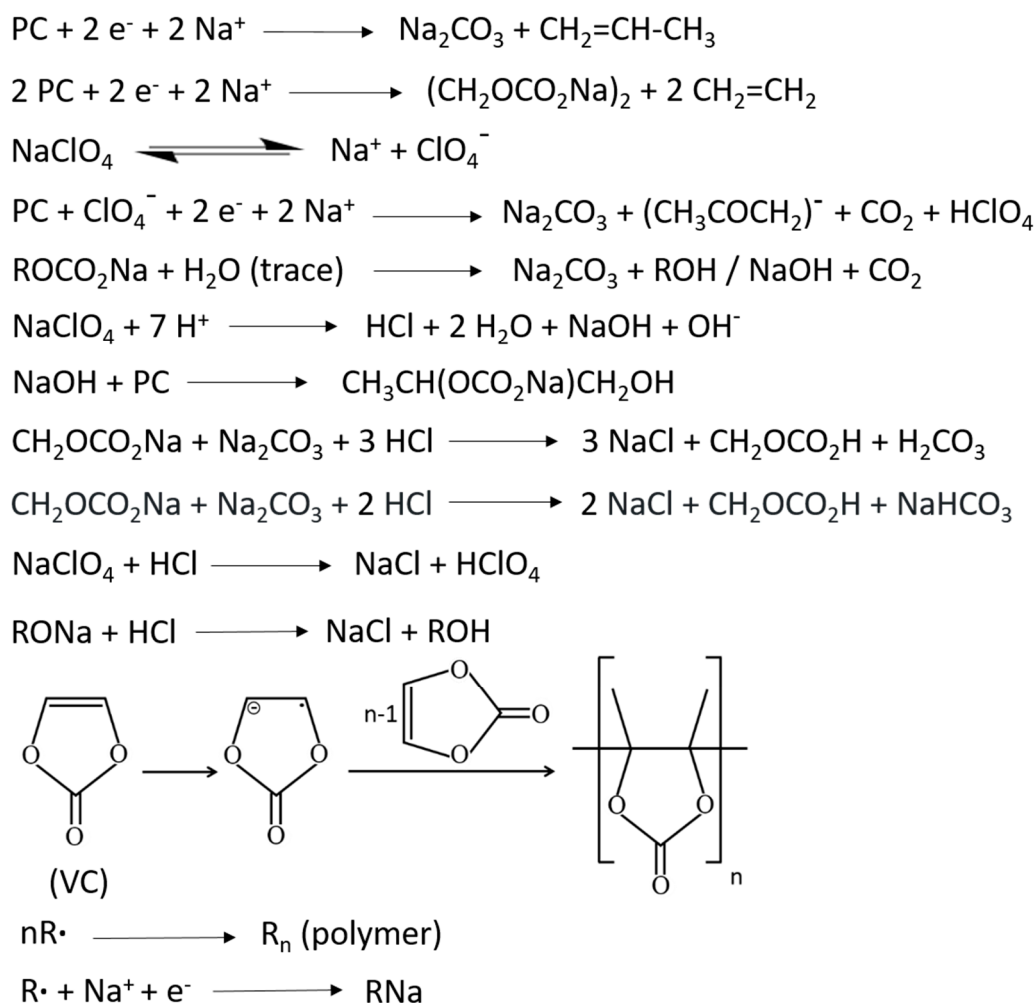


**Figure 8.** High-resolution XPS spectra of TiO<sub>2</sub> nanosheet electrodes after 30 cycles in PC-VC/NaClO<sub>4</sub> electrolyte solution for (a) survey, (b) C 1s, (c) O 1s, (d) Cl 2p, (e) Na 1s, (f) Ti 2p.

As presented in Scheme 1, two electron PC reduction in the presence of Na-ions leads to sodium carbonate (Na<sub>2</sub>CO<sub>3</sub>) and propylene (CH<sub>2</sub>=CH-CH<sub>3</sub>), whereas one electron reduction results in sodium alkyl carbonate (CH<sub>2</sub>OCO<sub>2</sub>Na)<sub>2</sub> and ethylene (CH<sub>2</sub>=CH<sub>2</sub>) formation. On the other hand, PC reaction with perchlorate anion (ClO<sub>4</sub><sup>-</sup>) forms hydrogen perchlorate (HClO<sub>4</sub>), carbon dioxide, and acetaldehyde radical [65]. The sodium alkyl carbonate produced interacting with the trace amounts of water present in the electrolyte could produce more sodium carbonate (where R = -CH<sub>3</sub>, or CH<sub>3</sub>-CH<sub>2</sub>), carbon dioxide, sodium hydroxide, and/or ROH species [66]. Protons generated by the dissociation of HClO<sub>4</sub> could react with NaClO<sub>4</sub> to form HCl, and sodium hydroxide (NaOH). Previously formed NaOH species reacted with the PC solvent to produce sodium alkyl carbonates [67]. Initially formed sodium alkyl carbonates react with the sodium carbonate and hydrochloric acid (HCl), and in the following steps generating sodium chloride (NaCl), desodiated alkyl carbonate (ROCO<sub>2</sub>H), and carbonic acid (H<sub>2</sub>CO<sub>3</sub>). This step can also form sodium bicarbonate (NaHCO<sub>3</sub>) instead of carbonic acid [66]. Most importantly, the increased reactivity of VC due to the presence of a double bond could form higher complexity sodiated polymers, such as sodium ethylene dicarbonate (NaO<sub>2</sub>CO-C<sub>2</sub>H<sub>4</sub>-OCO<sub>2</sub>Na), sodium butylene carbonate (CH<sub>2</sub>CH<sub>2</sub>OCO<sub>2</sub>Na)<sub>2</sub>, and poly-vinylene carbonate [41,64,66].



**Scheme 1.** Reduction reactions of PC-VC/NaClO<sub>4</sub> electrolyte solution.

Hence, the effect of solvents on the salt reduction can be investigated by comparing the Cl-concentration in the surface film. Among the carbonate solvents used in this case, VC is more reactive than PC towards electrochemical reduction, which leads to the difference in the SEI composition and properties [47]. In the case of PC/NaClO<sub>4</sub> electrolyte solution, high-resolution C 1s spectrum (Figure 7b) consisted of three distinct peaks located at 284.8 eV, 286.4 eV, and 289.6 eV, and characteristic of elemental carbon (C-C bonds), C-O-C/C-O groups of RONA, and C=O groups of ROCO<sub>2</sub>Na/Na<sub>2</sub>CO<sub>3</sub> species, respectively [28,68]. Signals corresponding to alkoxy groups were absent in the case of the VC-containing electrolyte solution (Figure 8b). The relative intensity of the ROCO<sub>2</sub>Na peaks was also less, which clearly indicated difference in the surface film composition. The O 1s spectra of the TiO<sub>2</sub> anodes cycled in VC-free electrolyte solution (Figure 7c) could be deconvoluted into individual peaks located at 531.0 eV, 532.6 eV, and 533.3 eV, corresponding to alkoxides, ether, and carbonate groups present in the surface film [49,68,69].

Due to the presence of similar functional groups, it was difficult to distinguish ROCO<sub>2</sub>Na present in VC-free and polycarbonate groups formed in VC-containing electrolyte solutions. However, slightly increased O 1s binding energies (531.2, 532.8, 533.5 eV, respectively) and increased width in the case of PC-VC/NaClO<sub>4</sub> indicated (Figure 8c) the presence of higher carbonate concentration in the SEI, possibly due to polycarbonate formation resulting from VC-decomposition. Increased oxygen and carbon content quantified from the high-resolution spectra (Table 1) also indicated the presence of higher carbonate content in the case of the VC-containing electrolyte solution. Hence, it can be concluded

that the surface films formed in both VC-free electrolyte solutions consisted of alkoxides, carbonates, and ether species. Whereas alkoxides were absent in the polycarbonate rich surface film formed in the VC-containing electrolyte solution.

High-resolution Cl 2p spectra related to both the VC-free and VC-containing electrolyte solutions exhibited similar features (Figures 7d and 8d). Individual peaks at 198.1 and 199.7 eV correspond to the Cl 2p<sub>3/2</sub> and Cl 2p<sub>1/2</sub> components, respectively, of inorganic chlorides (mainly NaCl) present in the surface film [70]. Signals corresponding to organic chlorides were not identified in the case of both electrolyte solutions. Increased salt (NaClO<sub>4</sub>) decomposition in the case of the VC-free electrolyte solution is also evidenced by the lower relative amount (Table 1) of inorganic chlorides in the surface film. This can be credited to the more pronounced ClO<sub>4</sub><sup>−</sup> reduction in the absence of highly reactive VC electrolyte additive. High-resolution Na 1s spectra in the case of both electrolyte solutions (Figures 7e and 8e) were identical, with a prominent peak at 1071.4 eV indicating the presence of NaCl in the surface film [70]. High-resolution Ti 2p spectra in the case of the surface films formed in both electrolyte solutions (Figures 7f and 8f) exhibited signals at 458.1 eV and 463.9 eV, which are characteristic of the Ti 2p<sub>3/2</sub> and Ti 2p<sub>1/2</sub> components of Ti<sup>4+</sup> ions [53].

This is in good agreement with the intercalation-type pseudocapacitive Na-ion storage mechanism we reported earlier for these anatase–bronze hybrid nanosheets [9]. Identical Na 1s and Ti 2p signals also verified a similar Na-ion storage mechanism of TiO<sub>2</sub> nanosheets in both VC-free and VC-containing electrolyte solutions. Increased Na and Ti concentration in the case of PC/NaClO<sub>4</sub> and PC-VC/NaClO<sub>4</sub> can be attributed to the enhanced NaClO<sub>4</sub> decomposition in the absence of VC, and superior transparency of polycarbonate based surface film for X-rays/electron beam, correspondingly.

Further surface chemical studies of the TiO<sub>2</sub> were performed by ATR-FTIR spectral measurements. FTIR spectra of non-cycled TiO<sub>2</sub> nanosheet electrodes, after cycling in VC-free and VC-containing electrolyte solutions (Figure 9a), exhibited clear differences in the surface chemical composition. Presence of ROCO<sub>2</sub>Na and Na<sub>2</sub>CO<sub>3</sub> as the major components resulting from PC reduction was evident from these spectra [64,67,70]. Peaks indicative of the symmetric and asymmetric stretch mode of C-O bond (ν C-O) present in ROCO<sub>2</sub>Na appeared in the 1450–1360 cm<sup>−1</sup> and 1650–1540 cm<sup>−1</sup> regions, respectively [67,71]. Scissoring vibrations for OCO<sub>2</sub><sup>−</sup> (δ OCO<sub>2</sub><sup>−</sup>) from the same species appeared at 871/877 cm<sup>−1</sup> for both electrolyte compositions [67,72]. C-H stretching (ν C-H) bands appear at higher frequencies between 2999 and 2930, which were identical to the previous reports for electrodes cycled in VC-free electrolytes [57,67]. Signals in the 2340–2350 cm<sup>−1</sup> range indicated the presence of atmospheric CO<sub>2</sub> [41]. Peaks at 1295 cm<sup>−1</sup>, 1075 cm<sup>−1</sup>, and 1067 cm<sup>−1</sup> belong to CO stretching/ CH<sub>3</sub> deformation coming from the organic species containing –ONa and/or –OCO<sub>2</sub>Na functional groups and double bonds [57,71]. Peaks originating from the carbonate group of Na<sub>2</sub>CO<sub>3</sub> (ν CO<sub>3</sub><sup>−2</sup>) were clearly visible at 1398 cm<sup>−1</sup>/1400 cm<sup>−1</sup> in the spectra [72]. These signals were absent in the spectra of the pristine TiO<sub>2</sub> electrode, confirming surface film formation only during the electrochemical charge–discharge process. Interestingly, additional peaks corresponding to PC/VC solvents and NaClO<sub>4</sub> salts are not visible in the case of the non-washed electrodes (Figure S4). This could be due to the dominant FTIR intensities of the SEI components compared to trace amounts of solvent and Na-salt. Similar FTIR spectra before and after washing confirmed that the SEI components were not damaged by acetonitrile solvent.

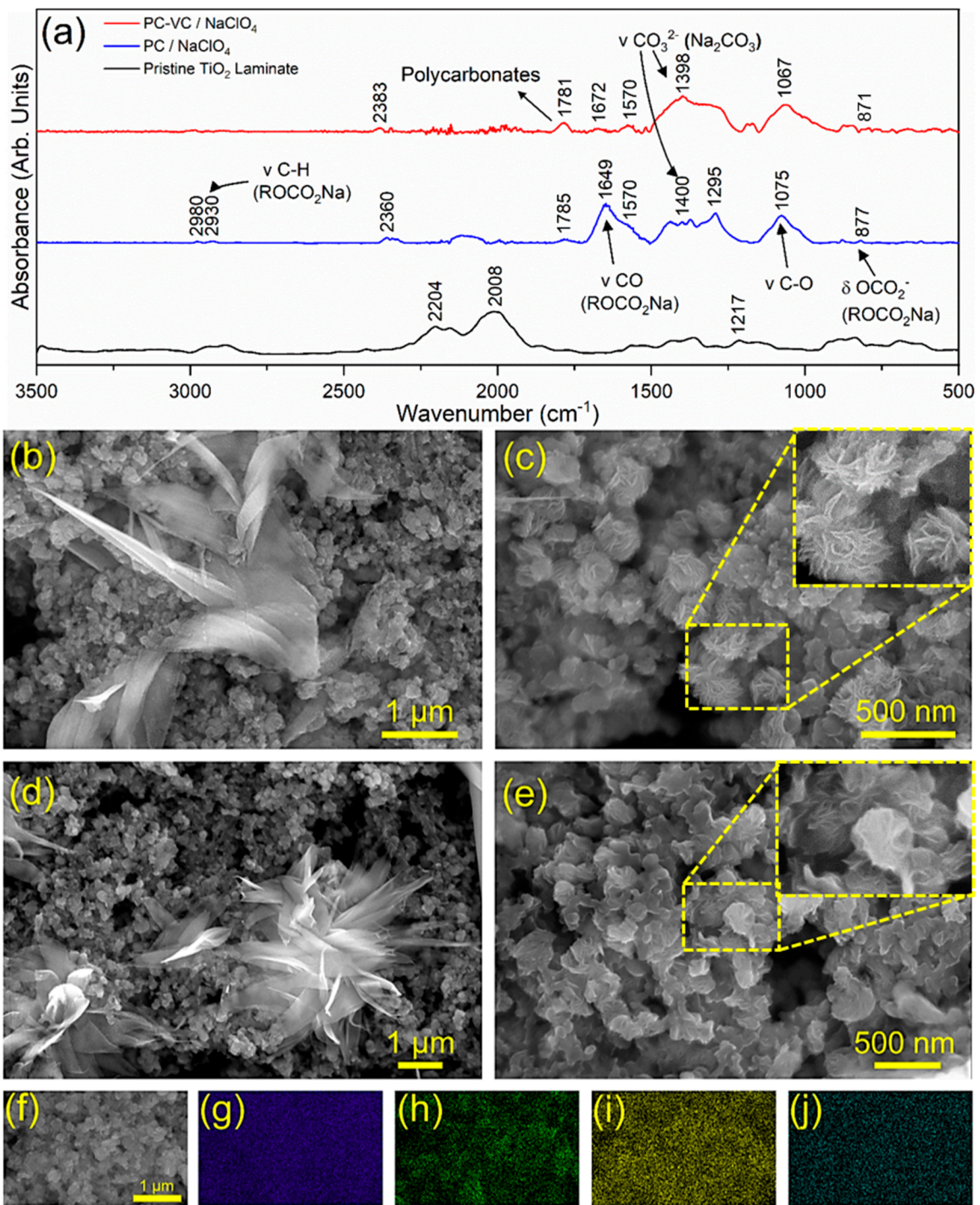


**Figure 9.** (a) ATR-FTIR spectra of non-cycled TiO<sub>2</sub> nanosheet electrodes, and after cycling in PC/NaClO<sub>4</sub> and PC-VC/NaClO<sub>4</sub> electrolyte solutions. Post-cycling SEM images of TiO<sub>2</sub> nanosheet electrodes in (b,c) PC/NaClO<sub>4</sub>, and (d,e) PC-VC/NaClO<sub>4</sub> electrolyte solution. (f) SEM image and (g–j) corresponding SEM-EDX elemental mapping of TiO<sub>2</sub> nanosheet electrodes after 30 cycles in PC-VC/NaClO<sub>4</sub> electrolyte solution.

Thus, the FTIR signals clearly demonstrated the formation of alkoxides and carbonates formed as a result of electrolyte decomposition (Scheme 1). The spectra related to PC/NaClO<sub>4</sub> and PC-VC/NaClO<sub>4</sub> electrolyte solutions are somewhat similar. The major difference between these spectra is the presence of polycarbonate peaks at around 1780 cm<sup>-1</sup> in the case of the VC-containing electrolyte [57]. It is indeed clear that VC-addition to PC/NaClO<sub>4</sub> electrolyte solution resulted in the formation of a polycarbonate rich surface

film, along with  $\text{Na}_2\text{CO}_3$  and  $\text{ROCO}_2\text{Na}$  species. Post-cycling SEM images (Figure 9b–e) of the  $\text{TiO}_2$  nanosheet anode confirmed their structural stability during the sodiation–desodiation process. Individual petals of the agglomerated  $\text{TiO}_2$  nanosheets were clearly visible through the surface films formed in both electrolyte solutions. EDX mapping of the  $\text{TiO}_2$  nanosheet anodes cycled in PC-VC/ $\text{NaClO}_4$  electrolyte solution (Figure 9f–j) also verified homogeneous SEI formation. Hence, it is clear that the difference in pseudocapacitance and cycling stabilities was a consequence of the different chemical compositions of the surface films rather than their thickness. This should be expected, considering the minimal volume changes of the  $\text{TiO}_2$  anode during the charge–discharge process, which is unlikely to form thicker SEI due to limited electrolyte consumption only in the initial cycles.

Surface chemical analysis results obtained from the ATR-FTIR measurements were in line with the XPS results discussed above. These spectral studies enabled us to differentiate the surface chemical aspects responsible for the increased pseudocapacitive Na-ion storage in VC-containing electrolyte solution. Surface film formation in the two different electrolyte solutions can be described as follows: In PC/ $\text{NaClO}_4$  electrolyte, PC reduction into  $\text{Na}_2\text{CO}_3$  and  $\text{ROCO}_2\text{Na}$  are the primary processes contributing to the surface film. There exists a competition between the PC and VC reduction in the case of PC-VC/ $\text{NaClO}_4$  electrolyte solution [47]. VC is the most reactive component, and surface films formed in this case constitute both VC polymerization and PC reduction products. Polycarbonates formed during the initial charge–discharge cycles, as a result of VC-decomposition, protect the highly reactive  $\text{TiO}_2$  anode from further reaction with the electrolyte solution. Improved passivation also resulted in the reduced decomposition of the  $\text{NaClO}_4$  salt, which is crucial for maintaining good ionic conductivity during extended charge–discharge cycles. Significantly improved pseudocapacitance resulted from the ultrafast Na-ion diffusion through the polycarbonate based surface film. It should be noted that improved electrochemical performance of graphite and silicon nanowire anodes in VC/ FEC containing electrolyte solutions has been observed previously [41]. Nevertheless, such drastic difference in the pseudocapacitive Na-ion storage mechanism has never been identified. In conclusion VC electrolyte additive resulted in excellent long term cycling stability and pseudocapacitive Na-ion storage, a consequence of the superior passivation and Na-ion transport properties of the polycarbonate-rich surface film.

#### 4. Conclusions

The effects of vinylene carbonate (VC) as an electrolyte additive on the surface chemistry and Na-ion storage mechanism was thoroughly investigated.  $\text{TiO}_2$  nanosheet anodes achieved enhanced long-term cycling stability and pseudocapacitance in VC-containing electrolyte solution compared to VC-free composition. FTIR and XPS surface chemical characterizations of  $\text{TiO}_2$  nanosheets cycled in VC-containing electrolyte solution confirmed the formation of polycarbonate rich surface film. Whereas, the VC-free electrolyte solution resulted in the formation of a sodium alkyl carbonate and sodium carbonate based surface film. The superior electrochemical performance of the  $\text{TiO}_2$  nanosheets in VC-containing electrolyte solution is credited to the faster pseudocapacitive Na-ion diffusion through the polycarbonate-based surface film. These results demonstrated that  $\text{TiO}_2$  nanosheet anodes in VC-containing alkyl carbonate electrolyte solutions can be utilized for advanced high-performance Na-ion batteries.

**Supplementary Materials:** The following are available online at <https://www.mdpi.com/2313-0105/7/1/1/s1>. Figure S1: High-resolution Raman spectra, Figure S2: Galvanostatic long cycling performance with different amount of VC additive, Figure S3: First cycle charge-discharge profiles of  $\text{TiO}_2$  nanosheet anodes, Figure S4: FTIR spectra of cycled  $\text{TiO}_2$  laminates without washing.

**Author Contributions:** R.R.M. and V.E., conceptualize the idea; R.R.M., performed materials synthesis and characterization; R.R.M. and V.E., together wrote the manuscript; V.E., also performed supervision of the work. All authors have read and agreed to the published version of the manuscript.

**Funding:** We thank IMDEA Materials Institute for generous start-up funding. Vinodkumar Etacheri acknowledges Spanish Ministry of Economy, Industry and Competitiveness (MINECO), Spanish Ministry of Science and Innovation, and Comunidad de Madrid for Juan de la Cierva fellowship (IJCI-2015-25488), Retos investigación project (MAT2017-84002-C2-2-R)/Ramon y Cajal fellowship (RYC-2018-025893-I), and Talent attraction fellowship (2016-T1/IND-1300) respectively.

**Data Availability Statement:** The data presented in this study are available within the article and/or supplementary material.

**Conflicts of Interest:** The authors declare no conflict of interest.

## References

1. Hwang, J.-Y.; Myung, S.-T.; Sun, Y.-K. Sodium-ion batteries: Present and future. *Chem. Soc. Rev.* **2017**, *46*, 3529–3614. [[CrossRef](#)] [[PubMed](#)]
2. Palomares, V.; Serras, P.; Villaluenga, I.; Hueso, K.B.; Carretero-González, J.; Rojo, T. Na-ion batteries, recent advances and present challenges to become low cost energy storage systems. *Energy Environ. Sci.* **2012**, *5*, 5884–5901. [[CrossRef](#)]
3. Etacheri, V.; Marom, R.; Elazari, R.; Salitra, G.; Aurbach, D. Challenges in the development of advanced Li-ion batteries: A review. *Energy Environ. Sci.* **2011**, *4*, 3243–3262. [[CrossRef](#)]
4. Madian, M.; Eychmüller, A.; Giebeler, L. Current advances in TiO<sub>2</sub>-based nanostructure electrodes for high performance lithium ion batteries. *Batteries* **2018**, *4*, 7. [[CrossRef](#)]
5. Dahbi, M.; Yabuuchi, N.; Fukunishi, M.; Kubota, K.; Chihara, K.; Tokiwa, K.; Yu, X.F.; Ushiyama, H.; Yamashita, K.; Son, J.Y.; et al. Black Phosphorus as a High-Capacity, High-Capability Negative Electrode for Sodium-Ion Batteries: Investigation of the Electrode/Electrolyte Interface. *Chem. Mater.* **2016**, *28*, 1625–1635. [[CrossRef](#)]
6. Battistel, A.; Palagonia, M.S.; Brogioli, D.; La Mantia, F.; Trócoli, R. Electrochemical Methods for Lithium Recovery: A Comprehensive and Critical Review. *Adv. Mater.* **2020**, *32*, 1905440. [[CrossRef](#)] [[PubMed](#)]
7. Rubio, S.; Maça, R.R.; Aragón, M.J.; Cabello, M.; Castillo-Rodríguez, M.; Lavela, P.; Tirado, J.L.; Etacheri, V.; Ortiz, G.F. Superior electrochemical performance of TiO<sub>2</sub> sodium-ion battery anodes in diglyme-based electrolyte solution. *J. Power Sources* **2019**, *432*, 82–91. [[CrossRef](#)]
8. Muñoz-Márquez, M.Á.; Saurel, D.; Gómez-Cámer, J.L.; Casas-Cabanas, M.; Castillo-Martínez, E.; Rojo, T. Na-Ion Batteries for Large Scale Applications: A Review on Anode Materials and Solid Electrolyte Interphase Formation. *Adv. Energy Mater.* **2017**, *7*, 1700463. [[CrossRef](#)]
9. Maça, R.R.; Cíntora Juárez, D.; Castillo Rodríguez, M.; Etacheri, V. Nanointerface-Driven Pseudocapacitance Tuning of TiO<sub>2</sub> Anode for High-Rate, Ultralong-Life and Enhanced Capacity Sodium-Ion Batteries. *Chem. Eng. J.* **2020**, *391*, 123598. [[CrossRef](#)]
10. Feng, W.; Maça, R.R.; Etacheri, V. High-Energy-Density Sodium-Ion Hybrid Capacitors Enabled by Interface-Engineered Hierarchical TiO<sub>2</sub> Nanosheet Anodes. *ACS Appl. Mater. Interfaces* **2020**, *12*, 4443–4453. [[CrossRef](#)]
11. Sanchez, J.S.; Maça, R.R.; Pendashteh, A.; Etacheri, V.; de la Peña O’Shea, V.A.; Castillo-Rodríguez, M.; Palma, J.; Marcilla, R. Hierarchical Co<sub>3</sub>O<sub>4</sub> nanorods anchored on nitrogen doped reduced graphene oxide: A highly efficient bifunctional electrocatalyst for rechargeable Zn–air batteries. *Catal. Sci. Technol.* **2020**, *10*, 1444–1457. [[CrossRef](#)]
12. Cao, Y.; Xiao, L.; Sushko, M.L.; Wang, W.; Schwenzler, B.; Xiao, J.; Nie, Z.; Saraf, L.V.; Yang, Z.; Liu, J. Sodium ion insertion in hollow carbon nanowires for battery applications. *Nano Lett.* **2012**, *12*, 3783–3787. [[CrossRef](#)] [[PubMed](#)]
13. Chen, J.; Zou, G.; Hou, H.; Zhang, Y.; Huang, Z.; Ji, X. Pinecone-like hierarchical anatase TiO<sub>2</sub> bonded with carbon enabling ultrahigh cycling rates for sodium storage. *J. Mater. Chem. A* **2016**, *4*, 12591–12601. [[CrossRef](#)]
14. Chao, D.; Zhu, C.; Yang, P.; Xia, X.; Liu, J.; Wang, J.; Fan, X.; Savilov, S.V.; Lin, J.; Fan, H.J.; et al. Array of nanosheets render ultrafast and high-capacity Na-ion storage by tunable pseudocapacitance. *Nat. Commun.* **2016**, *7*, 12122. [[CrossRef](#)]
15. Rubio, S.; Maça, R.R.; Ortiz, G.F.; Vicente, C.P.; Lavela, P.; Etacheri, V.; Tirado, J.L. Iron Oxide-Iron Sulfide Hybrid Nanosheets as High-Performance Conversion-Type Anodes for Sodium-Ion Batteries. *Appl. Energy Mater.* **2020**, *3*, 10765–10775. [[CrossRef](#)]
16. Yabuuchi, N.; Kubota, K.; Dahbi, M.; Komaba, S. Research development on sodium-ion batteries. *Chem. Rev.* **2014**, *114*, 11636–11682. [[CrossRef](#)]
17. Dahbi, M.; Nakano, T.; Yabuuchi, N.; Fujimura, S.; Chihara, K.; Kubota, K.; Son, J.Y.; Cui, Y.T.; Oji, H.; Komaba, S. Effect of Hexafluorophosphate and Fluoroethylene Carbonate on Electrochemical Performance and the Surface Layer of Hard Carbon for Sodium-Ion Batteries. *ChemElectroChem* **2016**, *3*, 1856–1867. [[CrossRef](#)]
18. Baggetto, L.; Keum, J.K.; Browning, J.F.; Veith, G.M. Germanium as negative electrode material for sodium-ion batteries. *Electrochem. Commun.* **2013**, *34*, 41–44. [[CrossRef](#)]
19. Kalubarme, R.S.; Lee, J.Y.; Park, C.J. Carbon Encapsulated Tin Oxide Nanocomposites: An Efficient Anode for High Performance Sodium-Ion Batteries. *ACS Appl. Mater. Interfaces* **2015**, *7*, 17226–17237. [[CrossRef](#)] [[PubMed](#)]
20. Qian, J.; Chen, Y.; Wu, L.; Cao, Y.; Ai, X.; Yang, H. High capacity Na-storage and superior cyclability of nanocomposite Sb/C anode for Na-ion batteries. *Chem. Commun.* **2012**, *48*, 7070–7072. [[CrossRef](#)]
21. Augustyn, V.; Come, J.; Lowe, M.A.; Kim, J.W.; Taberna, P.-L.; Tolbert, S.H.; Abruña, H.D.; Simon, P.; Dunn, B. High-rate electrochemical energy storage through Li+ intercalation pseudocapacitance. *Nat. Mater.* **2013**, *12*, 518–522. [[CrossRef](#)] [[PubMed](#)]

22. Longoni, G.; Pena Cabrera, R.L.; Polizzi, S.; D'Arienzo, M.; Mari, C.M.; Cui, Y.; Ruffo, R. Shape-Controlled TiO<sub>2</sub> Nanocrystals for Na-Ion Battery Electrodes: The Role of Different Exposed Crystal Facets on the Electrochemical Properties. *Nano Lett.* **2017**, *17*, 992–1000. [[CrossRef](#)] [[PubMed](#)]
23. Cargnello, M.; Gordon, T.R.; Murray, C.B. Solution-phase synthesis of titanium dioxide nanoparticles and nanocrystals. *Chem. Rev.* **2014**, *114*, 9319–9345. [[CrossRef](#)] [[PubMed](#)]
24. Oh, S.; Hwang, J.; Yoon, C.S.; Lu, J.; Amine, K.; Belharouak, I.; Sun, Y. High Electrochemical Performances of Microsphere C-TiO<sub>2</sub> Anode for Sodium-Ion Battery. *ACS Appl. Mater. Interfaces* **2014**, *6*, 11295–11301. [[CrossRef](#)] [[PubMed](#)]
25. Li, W.; Fukunishi, M.; Morgan, B.J.; Borkiewicz, O.J.; Chapman, K.W.; Pralong, V.V.; Maignan, A.; Lebedev, O.I.; Ma, J.; Groult, H.; et al. A Reversible Phase Transition for Sodium Insertion in Anatase TiO<sub>2</sub>. *Chem. Mater.* **2017**, *29*, 1836–1844. [[CrossRef](#)]
26. Ge, Y.; Jiang, H.; Zhu, J.; Lu, Y.; Chen, C.; Hu, Y.; Qiu, Y.; Zhang, X. High cyclability of carbon-coated TiO<sub>2</sub> nanoparticles as anode for sodium-ion batteries. *Electrochim. Acta* **2015**, *157*, 142–148. [[CrossRef](#)]
27. Chen, J.; Ding, Z.; Wang, C.; Hou, H.; Zhang, Y.; Wang, C.; Zou, G.; Ji, X. Black Anatase Titania with Ultrafast Sodium-Storage Performances Stimulated by Oxygen Vacancies. *ACS Appl. Mater. Interfaces* **2016**, *8*, 9142–9151. [[CrossRef](#)] [[PubMed](#)]
28. Goriparti, S.; Miele, E.; Prato, M.; Scarpellini, A.; Marras, S.; Monaco, S.; Toma, A.; Messina, G.C.; Alabastri, A.; De Angelis, F.; et al. Direct Synthesis of Carbon-Doped TiO<sub>2</sub>-Bronze Nanowires as Anode Materials for High Performance Lithium-Ion Batteries. *ACS Appl. Mater. Interfaces* **2015**, *7*, 25139–25146. [[CrossRef](#)]
29. Etacheri, V.; Kuo, Y.; Van Der Ven, A.; Bartlett, B.M. Mesoporous TiO<sub>2</sub>-B microflowers composed of (1-1 0) facet-exposed nanosheets for fast reversible lithium-ion storage. *J. Mater. Chem. A* **2013**, *1*, 12028–12032. [[CrossRef](#)]
30. Mehraeen, S.; Taşdemir, A.; Gürsel, S.A.; Yürüm, A. Homogeneous growth of TiO<sub>2</sub>-based nanotubes on nitrogen-doped reduced graphene oxide and its enhanced performance as a Li-ion battery anode. *Nanotechnology* **2018**, *29*, 255402. [[CrossRef](#)]
31. Su, D.; Dou, S.; Wang, G.; Su, D.; Dou, S.; Wang, G. Anatase TiO<sub>2</sub>: Better Anode Material than Amorphous and Rutile Phases of TiO<sub>2</sub> for Na-ion Batteries. *Chem. Mater.* **2015**, *27*, 6022–6029. [[CrossRef](#)]
32. Xu, Y.; Lotfabad, M.; Wang, H.; Farbod, B.; Xu, Z.; Mitlin, D. Nanocrystalline anatase TiO<sub>2</sub>: A new anode material for rechargeable sodium ion batteries. *Chem. Commun.* **2013**, *49*, 8973–8975. [[CrossRef](#)]
33. Wang, W.; Liu, Y.; Wu, X.; Wang, J.; Fu, L.; Zhu, Y.; Wu, Y.; Liu, X. Advances of TiO<sub>2</sub> as Negative Electrode Materials for Sodium-Ion Batteries. *Adv. Mater. Technol.* **2018**, *3*, 1800004. [[CrossRef](#)]
34. Usui, H.; Domi, Y.; Yoshioka, S.; Kojima, K.; Sakaguchi, H. Electrochemical Lithiation and Sodiation of Nb-Doped Rutile TiO<sub>2</sub>. *ACS Sustain. Chem. Eng.* **2016**, *4*, 6695–6702. [[CrossRef](#)]
35. Tanaka, Y.; Usui, H.; Domi, Y.; Ohtani, M.; Kobiro, K.; Sakaguchi, H. Mesoporous spherical aggregates consisted of Nb-doped anatase TiO<sub>2</sub> nanoparticles for Li and Na storage materials. *ACS Appl. Energy Mater.* **2019**, *2*, 636–643. [[CrossRef](#)]
36. Chen, C.; Wen, Y.; Ji, X.; Yan, M.; Mai, L.; Hu, P.; Shan, B.; Hu, X.; Huang, Y. Na<sup>+</sup> intercalation pseudocapacitance in graphene-coupled titanium oxide enabling ultra-fast sodium storage and long-term cycling. *Nat. Commun.* **2015**, *6*, 6929–6936. [[CrossRef](#)] [[PubMed](#)]
37. Chu, C.; Yang, J.; Zhang, Q.; Wang, N.; Niu, F.; Xu, X.; Yang, J.; Fan, W.; Qian, Y. Biphasic-Interface Enhanced Sodium Storage and Accelerated Charge Transfer: Flower-Like Anatase/Bronze TiO<sub>2</sub>/C as an Advanced Anode Material for Na-Ion Batteries. *ACS Appl. Mater. Interfaces* **2017**, *9*, 43648–43656. [[CrossRef](#)]
38. Peled, E.; Menkin, S. Review-SEI: Past, Present and Future. *J. Electrochem. Soc.* **2017**, *164*, A1703–A1719. [[CrossRef](#)]
39. Huang, Y.; Zhao, L.; Li, L.; Xie, M.; Wu, F.; Chen, R. Electrolytes and Electrolyte/Electrode Interfaces in Sodium-Ion Batteries: From Scientific Research to Practical Application. *Adv. Mater.* **2019**, *31*, 1808393. [[CrossRef](#)] [[PubMed](#)]
40. Ponrouch, A.; Marchante, E.; Courty, M.; Tarascon, J.-M.; Palacín, M.R. In search of an optimized electrolyte for Na-ion batteries. *Energy Environ. Sci.* **2012**, *5*, 8572–8583. [[CrossRef](#)]
41. Etacheri, V.; Haik, O.; Goffer, Y.; Roberts, G.A.; Stefan, I.C.; Fasching, R.; Aurbach, D. Effect of Fluoroethylene Carbonate (FEC) on the Performance and Surface Chemistry of Si-Nanowire Li-Ion Battery Anodes. *Langmuir* **2012**, *28*, 965–976. [[CrossRef](#)] [[PubMed](#)]
42. Song, J.; Xiao, B.; Lin, Y.; Xu, K.; Li, X. Interphases in Sodium-Ion Batteries. *Adv. Energy Mater.* **2018**, *8*, 1703082. [[CrossRef](#)]
43. Peled, E.; Patolsky, F.; Golodnitsky, D.; Freedman, K.; Davidi, G.; Schneier, D. Tissue-like Silicon Nanowires-Based Three-Dimensional Anodes for High-Capacity Lithium Ion Batteries. *Nano Lett.* **2015**, *15*, 3907–3916. [[CrossRef](#)] [[PubMed](#)]
44. Ushirogata, K.; Sodeyama, K.; Tateyama, Y.; Okuno, Y.; Tateyama, Y. Additive Effect on Reductive Decomposition and Binding of Carbonate-Based Solvent toward Solid Electrolyte Interphase Formation in Lithium-Ion Battery. *J. Am. Chem. Soc.* **2013**, *135*, 11967–11974. [[CrossRef](#)] [[PubMed](#)]
45. Jaumann, T.; Balach, J.; Langklotz, U.; Sauchuk, V.; Fritsch, M.; Michaelis, A.; Telteviskij, V.; Mikhailova, D.; Oswald, S.; Klose, M.; et al. Lifetime vs. rate capability: Understanding the role of FEC and VC in high-energy Li-ion batteries with nano-silicon anodes. *Energy Storage Mater.* **2017**, *6*, 26–35. [[CrossRef](#)]
46. Wang, L.; Światowska, J.; Dai, S.; Cao, M.; Zhong, Z.; Shen, Y.; Wang, M. Promises and challenges of alloy-type and conversion-type anode materials for sodium-ion batteries. *Mater. Today Energy* **2019**, *11*, 46–60. [[CrossRef](#)]
47. Liu, Q.; Mu, D.; Wu, B.; Wang, L.; Gai, L.; Wu, F. Density Functional Theory Research into the Reduction Mechanism for the Solvent/Additive in a Sodium-Ion Battery. *ChemSusChem* **2017**, *10*, 786–796. [[CrossRef](#)]
48. Tao, H.; Zhou, M.; Wang, K.; Cheng, S.; Jiang, K. Glycol Derived Carbon-TiO<sub>2</sub> as Low Cost and High Performance Anode Material for Sodium-Ion Batteries. *Sci. Rep.* **2017**, *7*, 43895–43901. [[CrossRef](#)]

49. Song, W.; Jiang, Q.; Xie, X.; Brookfield, A.; McInnes, E.J.L.; Shearing, P.R.; Brett, D.J.L.; Xie, F.; Riley, D.J. Synergistic storage of lithium ions in defective anatase/rutile TiO<sub>2</sub> for high-rate batteries. *Energy Storage Mater.* **2019**, *22*, 441–449. [[CrossRef](#)]
50. Yang, P.D.; Zhao, D.Y.; Margolese, D.I.; Chmelka, B.F.; Stucky, G.D. Generalized syntheses of large-pore mesoporous metal oxides with semicrystalline frameworks. *Lett. to Nat.* **1998**, *396*, 152–155. [[CrossRef](#)]
51. Yu, X.; Kim, B.; Kim, Y.K. Highly enhanced photoactivity of anatase TiO<sub>2</sub> nanocrystals by controlled hydrogenation-induced surface defects. *ACS Catal.* **2013**, *3*, 2479–2486. [[CrossRef](#)]
52. Beuvier, T.; Richard-plouet, M.; Brohan, L. Accurate Methods for Quantifying the Relative Ratio of Anatase and TiO<sub>2</sub>(B) Nanoparticles. *J. Phys. Chem. C* **2009**, *113*, 13703–13706. [[CrossRef](#)]
53. Wu, L.; Bresser, D.; Buchholz, D.; Giffi, G.; Castro, C.R.; Ochel, A.; Passerini, S.; Giffin, G.A.; Castro, C.R.; Ochel, A.; et al. Unfolding the Mechanism of Sodium Insertion in Anatase TiO<sub>2</sub> Nanoparticles. *Adv. Energy Mater.* **2014**, *5*, 1401142. [[CrossRef](#)]
54. Zhang, Y.; Pu, X.; Yang, Y.; Zhu, Y.; Hou, H.; Jing, M.; Yang, X.; Chen, J.; Ji, X. An Electrochemical Investigation of Rutile TiO<sub>2</sub> Microspheres Anchored by Nanoneedle Clusters for its Sodium Storage. *Phys. Chem. Chem. Phys.* **2015**, *17*, 15764–15770. [[CrossRef](#)] [[PubMed](#)]
55. Randles, J.E.B. Kinetics of Rapid Electrode Reactions. *Discuss. Faraday Soc.* **1947**, *1*, 11–19. [[CrossRef](#)]
56. Mogi, R.; Inaba, M.; Jeong, S.-K.; Iriyama, Y.; Abe, T.; Ogumi, Z. Effects of Some Organic Additives on Lithium Deposition in Propylene Carbonate. *J. Electrochem. Soc.* **2002**, *149*, A1578–A1583. [[CrossRef](#)]
57. Aurbach, D.; Gamolsky, K.; Markovsky, B.; Gofer, Y.; Schmidt, M.; Heider, U. On the use of vinylene carbonate (VC) as an additive to electrolyte solutions for Li-ion batteries. *Electrochim. Acta* **2002**, *47*, 1423–1439. [[CrossRef](#)]
58. Augustyn, V.; Simon, P.; Dunn, B. Pseudocapacitive oxide materials for high-rate electrochemical energy storage. *Energy Environ. Sci.* **2014**, *7*, 1597–1614. [[CrossRef](#)]
59. Babu, B.; Shaijumon, M.M. High performance sodium-ion hybrid capacitor based on Na<sub>2</sub>Ti<sub>2</sub>O<sub>4</sub>(OH)<sub>2</sub> nanostructures. *J. Power Sources* **2017**, *353*, 85–94. [[CrossRef](#)]
60. Lesel, B.K.; Cook, J.B.; Yan, Y.; Lin, T.C.; Tolbert, S.H. Using Nanoscale Domain Size to Control Charge Storage Kinetics in Pseudocapacitive Nanoporous LiMn<sub>2</sub>O<sub>4</sub> Powders. *ACS Energy Lett.* **2017**, *2*, 2293–2298. [[CrossRef](#)]
61. De La Llave, E.; Borgel, V.; Park, K.J.; Hwang, J.Y.; Sun, Y.K.; Hartmann, P.; Chesneau, F.F.; Aurbach, D. Comparison between Na-Ion and Li-Ion Cells: Understanding the Critical Role of the Cathodes Stability and the Anodes Pretreatment on the Cells Behavior. *ACS Appl. Mater. Interfaces* **2016**, *8*, 1867–1875. [[CrossRef](#)] [[PubMed](#)]
62. Costentin, C.; Porter, T.R.; Save, J. How Do Pseudocapacitors Store Energy? Theoretical Analysis and Experimental Illustration. *ACS Appl. Mater. Interfaces* **2017**, *9*, 8649–8658. [[CrossRef](#)] [[PubMed](#)]
63. El Ouatani, L.; Dedryvère, R.; Siret, C.; Biensan, P.; Gonbeau, D. Effect of Vinylene Carbonate Additive in Li-Ion Batteries: Comparison of LiCoO<sub>2</sub>/C, LiFePO<sub>4</sub>/C, and LiCoO<sub>2</sub>/Li<sub>4</sub>Ti<sub>5</sub>O<sub>12</sub> Systems. *J. Electrochem. Soc.* **2009**, *156*, A468–A477. [[CrossRef](#)]
64. Kumar, H.; Detsi, E.; Abraham, D.P.; Shenoy, V.B. Fundamental Mechanisms of Solvent Decomposition Involved in Solid-Electrolyte Interphase Formation in Sodium Ion Batteries. *Chem. Mater.* **2016**, *28*, 8930–8941. [[CrossRef](#)]
65. Leggesse, E.G.; Lin, R.T.; Teng, T.F.; Chen, C.L.; Jiang, J.C. Oxidative decomposition of propylene carbonate in lithium ion batteries: A DFT study. *J. Phys. Chem. A* **2013**, *117*, 7959–7969. [[CrossRef](#)]
66. Fondard, J.; Irisarri, E.; Courrèges, C.; Palacin, M.R.; Ponrouch, A.; Dedryvère, R. SEI Composition on Hard Carbon in Na-Ion Batteries After Long Cycling: Influence of Salts (NaPF<sub>6</sub>, NaTFSI) and Additives (FEC, DMCF). *J. Electrochem. Soc.* **2020**, *167*, 070526. [[CrossRef](#)]
67. Moshkovich, M.; Gofer, Y.; Aurbach, D. Investigation of the Electrochemical Windows of Aprotic Alkali Metal (Li, Na, K) Salt Solutions. *J. Electrochem. Soc.* **2001**, *148*, E155–E167. [[CrossRef](#)]
68. Aurbach, D.; Weissman, I.; Schechter, A.; Cohen, H. X-ray Photoelectron Spectroscopy Studies of Lithium Surfaces Prepared in Several Important Electrolyte Solutions. A Comparison with Previous Studies by Fourier Transform Infrared Spectroscopy. *Langmuir* **1996**, *12*, 3991–4007. [[CrossRef](#)]
69. Herstedt, M.; Abraham, D.P.; Kerr, J.B.; Edström, K. X-Ray Photoelectron Spectroscopy of Negative Electrodes from High-Power Lithium-Ion Cells Showing Various Levels of Power Fade. *Electrochim. Acta* **2004**, *49*, 5097–5110. [[CrossRef](#)]
70. Muñoz-Márquez, M.A.; Zarrabeitia, M.; Castillo-Martínez, E.; Eguía-Barrio, A.; Rojo, T.; Casas-Cabanas, M. Composition and evolution of the solid-electrolyte interphase in Na<sub>2</sub>Ti<sub>3</sub>O<sub>7</sub> electrodes for Na-Ion batteries: XPS and Auger parameter analysis. *ACS Appl. Mater. Interfaces* **2015**, *7*, 7801–7808. [[CrossRef](#)]
71. Matsuta, S.; Asada, T.; Kitaura, K. Vibrational Assignments of Lithium Alkyl Carbonate and Lithium Alkoxide in the Infrared Spectra. *J. Electrochem. Soc.* **2000**, *147*, 1695–1702. [[CrossRef](#)]
72. Tsubouchi, S.; Domi, Y.; Doi, T.; Ochida, M.; Nakagawa, H.; Yamanaka, T.; Abe, T.; Ogumi, Z. Spectroscopic Characterization of Surface Films Formed on Edge Plane Graphite in Ethylene Carbonate-Based Electrolytes Containing Film-Forming Additives. *J. Electrochem. Soc.* **2012**, *159*, A1786–A1790. [[CrossRef](#)]